energies

Review

Optical Diagnostics for Solid Rocket Plumes Characterization: A Review

Angelica Maria Toscano, Marco Rocco Lato, Donato Fontanarosa and Maria Grazia De Giorgi *

Department of Engineering for Innovation, University of Salento, 73100 Lecce, Italy;
angelicamaria.toscano@unisalento.it (A.M.T.); marcorocco.lato@unisalento.it (M.R.L.);
donato.fontanarosa@unisalento.it (D.F.)
* Correspondence: mariagrazia.degiorgi@unisalento.it

Abstract: In recent decades, solid fuel combustion propulsion of spacecraft has become one of the most popular choices for rocket propulsion systems. The reasons for this success are a wide range of applications, lower production costs, simplicity, and safety. The rocket's plumes leave the nozzle at high temperatures; hence, the knowledge of produced infrared (IR) emissions is a crucial aspect during the design and tests of the rocket motors. Furthermore, rocket plume composition is given by N_2, H_2, H_2O, CO and CO_2, while solid rocket motors (SRM) additionally inject some solid particles, given by metal fuel additives in the propellant grain, i.e., aluminum oxide (Al_2O_3) particles. The main issue is the detection of the particles remaining in the atmosphere due to the exhaust gas of the solid rocket propulsion system that could have effects on ozone depletion. The experimental characterization of SRM plumes in the presence of alumina particles can be conducted using different optical techniques. The present study aims to review the most promising ones with a description of the optics system and their potential applications for SRM plume measurements. The most common measurement techniques are infrared spectroscopy imaging, IR imaging. UV–VIS measurements, shadowgraph, and Schlieren optical methods. The choice of these techniques among many others is due to the ability to study the plume without influencing the physical conditions existing in and around the study object. This paper presents technical results concerning the study of rocket engines plumes with the above-mentioned methods and reveals the feasibility of the measurement techniques applied.

Keywords: rocket plume; optical techniques; flow diagnostics; nozzle; spectroscopy; IR signature; Schlieren; shadowgraph; digital inline holography

check for updates

Citation: Toscano, A.M.; Lato, M.R.; Fontanarosa, D.; De Giorgi, M.G. Optical Diagnostics for Solid Rocket Plumes Characterization: A Review. *Energies* **2022**, *15*, 1470. https://doi.org/10.3390/en15041470

Academic Editor: Francesco Creta

Received: 5 January 2022
Accepted: 11 February 2022
Published: 17 February 2022

1. Introduction

In rocket motors, hot gases are produced in the combustion chamber and expelled through the nozzle and thus interact with the air. In the mixing layer, there occurs the afterburning reaction due to some oxygen particles that are entrained into the plume; therefore, there is a significant rise in temperature as well as in radiation intensity for the exhaust gases. Hence, rocket engine plumes present high temperatures, high speeds, and intense radiation. For these reasons, the plume temperature is an essential parameter of rocket engine performance that permits understanding internal combustion conditions and overall engine performance. In recent decades, solid fuel combustion propulsion of spacecraft has become one of the most popular choices for rocket propulsion systems due to lower production costs, simplicity, and safety.

Typical oxidizers of solid rocket motors (SRMs) are solid aluminum fuel and ammonium perchlorate and are sometimes hydrocarbons and hydroxyl-terminated polybutadiene (HTPB). The SRM exhaust plume contains several compounds, i.e., CO, N_2, H_2, H_2O, and CO_2, and additional solid particles. Generally, in the solid propellant composition, there are additives, i.e., boron and aluminum, which increase rocket thrust. The aluminum reacts with combustion products and produces alumina (Al_2O_3) that is collected on the burning particles surface and represents one of the main sources of high thermal infrared emission in the rocket plume; the proportion of the Al_2O_3 depends on the type of propellant used [1].

Hence, a detailed description of radiative particles properties, as well as the measurements of the exhaust plume temperature and its distribution, are of great importance, because radiative heat transfer leads to a rise in the rocket surface temperature by several hundred degrees, with a deterioration of the rocket base. Moreover, the rocket plume is essential in target detection and identification.

The radiation from the plume is in the visible, infrared, and ultraviolet wavelength range. The infrared radiation is mostly given by the gas radiation of some combustion products as CO_2 and H_2O and the contribution of solid particles that emit in a continuous spectrum. CO_2 has three principal spectral bands, 2.6~2.8 μm, 4.1~4.5 μm, and 12.5~17.0 μm, and H_2O has three main spectral bands, 2.5~2.8 μm, 5.6~7.6 μm, and 12.0~17.0 μm. Previous studies have found that rocket plume radiation is mainly present in two spectral bands, at 4.3 and 2.8 μm [2].

The Al_2O_3 particles in the exhaust plume emit in the ultraviolet spectral range because of the high temperature that reaches values in the range of 2000–3000 K. Moreover, high-temperature iron oxide particles are emitted in the ultraviolet spectrum. Finally, the unburned fuels in the exhaust plume generate high amounts of C, N, and H, which produce free photons by chemical reactions with ultraviolet radiation [3].

The present article provides a comprehensive review of the numerous experimental techniques used to characterize the rocket plume and to investigate the physical presence of alumina particles in the plume of the solid rocket propulsion. The review also presents the description of the most recent advancements concerning the instrumentation and the different measurement approaches. Regarding the investigation of the alumina particles in the exhaust gases of solid rocket motors, the present work focuses on the optical techniques owning the characteristics of non-intrusiveness and relatively long distance between the experimental equipment and the extremely hot supersonically expanding gas, to ensure safety during operation.

2. Solid Rocket Plume: Optical and Radiative Properties of Alumina Particles

2.1. Propellants

The selection of propellant type is essential in a solid rocket motor design. SRM propellants should ensure high specific impulse, good ignition performance and combustion stability, elevated density, simplicity in the manufacturing, low cost, and great aging properties. Furthermore, they should generate gases with low smoke particles. In addition, they should ensure appropriate thermophysical and mechanical properties for each operational and storage condition.

Solid propellants are usually grouped as homogeneous solid propellants and heterogeneous solid propellants. The first ones are then classified as single-base (SB), double-base (DB), triple-base (TB), composite modified double base (CMDB).

The homogeneous solid propellants are:

- SB propellants that contain nitrocellulose (NC) that has been gelatinized in acetone or in alcohol–ether solvent mixture with the addition of additives to improve the quality of the propellant powder.
- DB propellants are made of two monopropellant fuels, a high-energy monopropellant and a lower-energy stabilizing monopropellant. Mostly, the nitroglycerin (NG) is dispersed in a nitrocellulose gel and solidified with additives, i.e., aluminum, to improve rocket performance; however, this leads to metal oxide nucleation in the plume.
- TB propellants are basically DB propellants with added 1-nitroguanidine (NQ). NQ contains hydrogen atoms that reduce the average molecular weight of the combustion products.
- CMDB are constituted by an NC/NG double-base propellant with the addition of solids (usually ammonium perchlorate and aluminum). The structure of CMDB is

slightly heterogeneous, with physicochemical characteristics of both composite and homogeneous propellants [4].

Heterogeneous propellants are constituted by a combination of oxidizer particles, as ammonium perchlorate (AP) and ammonium nitrate (AN), in a matrix of hydrocarbon-based polymers, i.e., hydroxyl-terminated polybutadiene (HTPB), carboxy terminated polybutadiene (CTPB), and polybutadiene acrylonitrile (PBAN). Usually, a high specific impulse is obtained by high concentrations of oxidizers and the addition of aluminum particles.

Metal fuels (i.e., aluminum and boron) are commonly included in the grain [5–7] to enhance the performance in terms of heat of combustion, propellant density, combustion, and specific impulse. Small aluminum particles with a diameter between 5 and 60 µm are usually used, in the range of 14–20% of the propellant weight.

Two-phase flow losses could be generated by the coalescence and agglomeration of micron-sized Al particles on the propellant surface; this reduces the flow velocity and causes losses in the thermal energy transfer of the flow [8]. The increase in the oxide particle size permits a decrease in the two-phase flow losses. Nevertheless, particles with larger granularity produce a variety of additional complications, such as incomplete combustion with a reduction of energy release, and erosion caused by collision into walls that may lead to degradation of the rocket propulsion performance and safety questions [9].

2.2. Optical and Radiative Properties of Alumina Particles

Rocket engines produce high-temperature two-phase plumes created by combustion gases and solid particles with a significant release of infrared energy. This permits the detection, tracking, and identification of rocket targets. During SRM operation, the temperature in the combustion chamber can reach temperature values up to 3800 K and pressures of 10 MPa. The combustion of aluminum produces micron-sized condensed phase particles that have an impact on internal flow and heat transfer, with two-phase flow losses, particles erosion, and radiative heating [10].

Consequently, significant effort has been addressed to characterize the optical properties of these solid particles and the absorption index and refractive index to permit correct estimation of radiative heating.

The different data available in previous articles and studies on the alumina absorption index have different values in terms of intensity and temperatures under investigation.

Some data have been obtained from the analysis of alumina taken from real SRM plumes or in experimental campaigns under temperature conditions close to nearly 3000 K; hence, their impurities were present in the particles, and the obtained absorption index value was elevated [11,12]. Other studies used single-crystal alumina in an almost pure state and heated under an aerodynamic levitation condition [13]. Under these conditions, the measured absorption index value was low, and the test temperature was also lower than the melting point. The measured available data have been used to implement analytical expressions for the absorption index with a dependence on temperature and wavelength [14]. The difference between the data obtained under real rocket conditions and the ones for single crystal alumina is significant. The following relationships are usually used for the estimation of the absorption index k and the refractive index n:

Bakhir et al. (1977):

$$k = 0.002\left(0.06\lambda^2 + 0.7\lambda + 1\right)\exp(1.847(T^* - 2.95)) \tag{1}$$

$$T^* = \frac{T}{1000} \tag{2}$$

Kuzmin et al. (2015):

$$\log k = -2.19 + 0.089\lambda^{0.95} - 0.00056(3200 - T)\lambda^{-0.45} \tag{3}$$

$$n = 1.747 + 0.0066\lambda - 0.0068\lambda^2 + 0.00003 \times T \tag{4}$$

Dombrovsky (1996):

$$n = \left[1 + \lambda^2\left(\frac{1.024}{\lambda^2 - 0.00376} + \frac{1.058}{\lambda^2 - 0.01225} + \frac{5.28}{\lambda^2 - 321.4}\right)\right]^{0.5} \tag{5}$$

$$T^* = \frac{T}{1000} \times [1 + 0.0202(T^* - 0.473)] \tag{6}$$

In the previous formulas, T is the temperature in K and λ the wavelength.

Figure 1 shows the absorption index numbers at different temperature values and over the wavelength from 0.5 to 8 µm based on the two analytical relationships. It is clearly shown that there are differences in the two analytical relationships of the absorption coefficient of alumina in function of temperature and spectral wavelength. The differences between the two different models increase with the rise in the wavelength. The refractive index calculated with the analytical expression of Kuzmin et al. [11] is approximately 1.8 in the wavelength range from 0.5 to 8 µm.

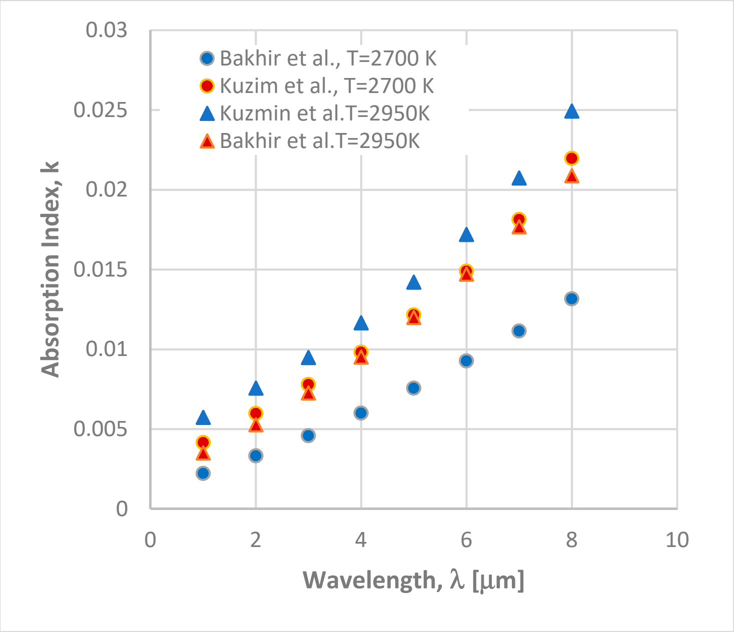

Figure 1. Analytical absorption coefficient in function of the wavelength and temperature [11,15].

The complex Mie scattering theory [16] can be used to calculate the radiative properties of micron-sized alumina. These calculations depend on the wavelength and particle size. The wavelength range could be assumed from 0.5 to 5 µm because the plume thermal emission mainly occurs in this range [17]. Regarding the particle size in the plume, individual aluminum particles in the propellant have typical initial sizes between 5 and 40 µm [18]; however, during combustion, they may melt together and form large agglomerates [19]. Finally, larger agglomerates could produce Al_2O_3 caps, vaporizing near 3240 K, and small particles (~1 µm) of Al_2O_3 could be expelled as smoke [19,20]. Previous studies established that the particle size in the plume is rarely greater than 15 µm ([21,22]) with a log-normal distribution [23].

In [10], the effect of the particle number density on the plume radiative properties, i.e., the absorption and scattering coefficients, was evaluated. The absorption and scattering coefficients were calculated using the estimated absorption index k [11,15] and the refractive index n [15,24]. Figure 2 shows these properties for a single-sized particle in the plume.

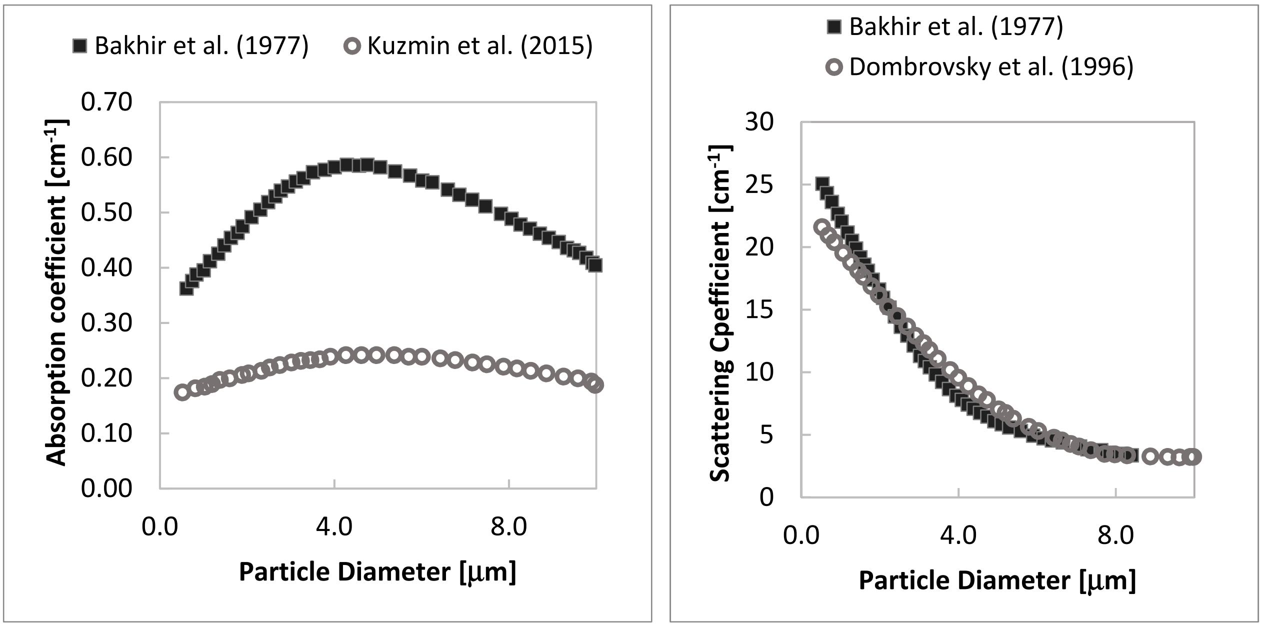

Figure 2. Absorption coefficient (on the left) and scattering coefficient (on the right) for different alumina particle diameters. Reprinted with permission from [10,11,15].

3. Spectroscopic Methods: FTIR, UV–VIS and AEM

Spectroscopy techniques allow for the study of the exhaust plume for different rocket working conditions and to obtain accurate results. The distinctive advantage of the spectroscopic method is proper study of the emission or absorption spectra of the plume rocket without interfering with the physical conditions of the plume and the surrounding environment. The purpose of this analysis is to obtain information on the rocket engine by measuring the radiation spectrum of its plume. Electromagnetic waves for simplicity are assumed to be made up of particles with energy, called photons. Spectroscopy exploits the phenomenon of increased energy of matter that occurs when the object under examination absorbs a photons beam. A sample increases its energy when it absorbs a photon. The particles energy expressed in Joules, is described in Equation (7):

$$E = h\nu = \frac{hc}{\lambda} = hc\overline{\nu} \tag{7}$$

where the symbol h is the Planck's constant equal to 6.626 × 10^{-34} Js. The energy of each photon E is given by the product of the frequency ν by the number of Planck's h. The frequency is equal to $\nu = c/\lambda$, where c is the light speed, and λ is the wavelength of the light emitted. The spectroscopic measurement is based on the detection of variations in the electromagnetic radiation characteristics when this passes through the sample and interacts with it. The spectroscope detects the decrease in electromagnetic waves passing through the sample. The matter crossed by electromagnetic waves absorbs part of the radiation and transmits the remaining part. Therefore, the radiation that is transmitted has a lower intensity. This phenomenon is described by two magnitudes the transmittance (T) and absorbance (A). These variables are linked through Beer's law that permits estimation of the concentration of the species:

$$A = -\log T = \varepsilon b C \tag{8}$$

The absorbance depends on the depth of the sample (b) and its concentration (C), the proportionality constant ε is called molar absorptivity and is specific for a compound at a given wavelength.

The spectroscopic methods are based on the detection of the emission because when the electromagnetic waves passing through the sample atom are excited, the atoms emit a photon to return to their original state. Photon emission detection is a method used in spectroscopy. The main techniques widely used in the study of the exhausted gasses of rocket engines are UV–VIS spectroscopy and IR spectroscopy, in particular FTIR (Fourier transform infrared) spectroscopy.

3.1. Fourier Transform Infrared Spectroscopy

FTIR spectroscopy has several advantages, the most important is the possibility of having spectral measurements in real-time due to the collection of a broad range of wavelengths using an interferometer, which is the heart of every FTIR instrument (Figure 3) [25].

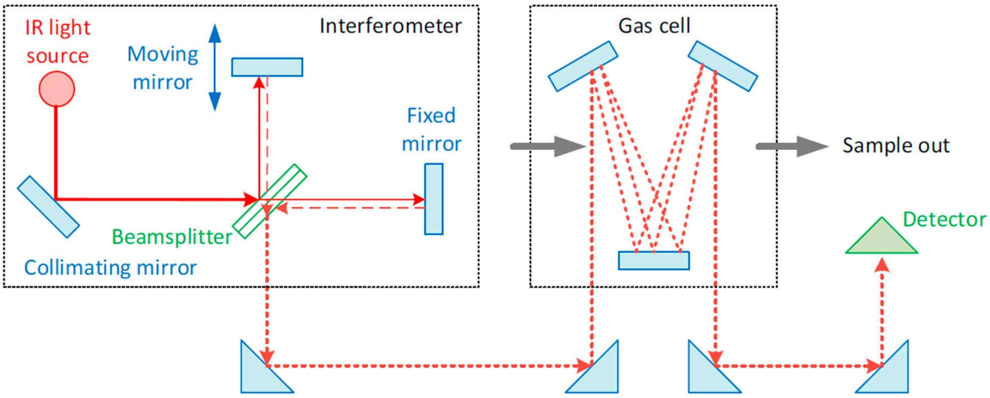

Figure 3. Diagram of the principle of operation of an infrared FTIR spectroscope. Reprinted with permission from Ref. [25] (2021).

The Michelson interferometer is the first model of interferometers, and it is the most commonly used. Using a collimating mirror, the sensor makes the light rays coming from the sample parallel, and the light acts on a beam splitter, where some of the rays are transmitted and the others are reflected. The transmitted light splits and hits both a fixed mirror and a moving mirror. The two light beams are recombined into a single light beam due to the reflection of the two mirrors back to the beam splitter. The single-beam passes through the object under examination and finally strikes the detector. In the interferometer, there are two rays, one has a fixed length and the other continuously changes its length due to the moving mirror, the interference between these two signals is the result obtained with the interferometer. The results are shown through an interferogram, and to obtain a spectrum, the signal must be mathematically transformed with Fourier. This is one of the spectroscopy methods used in the study of W. Gill et al. [26] in the Sandia National Laboratories to measure plume temperatures of a rocket solid motor in an off-design situation. The study deals with the analysis of the thermochemical and physical features of the plume and the definition of environmental conditions around the plume. During the experiment, the propellant was burned at design condition, i.e., at atmospheric pressure, with metal droplets in the hot exhaust gases. The use of spectroscopy permits one to characterize the temperature of the components of the exhaust plume. In this study, when the solid propellant burns, there is a reaction of the ammonium perchlorate (NH_4ClO_4), with the generation of multiple gases, including CO_2, H_2O and HCl. Nexus 670 is the spectrometer based on Fourier Transformation that was used to measure HCL concentrations. The results provided a calculated temperature of the order from 1100 to 1400 K. Comparing these latter results with the temperature obtained in the tests conducted in the ovens in the laboratory, there is a difference of 100 K between the temperatures. Therefore, the FTIR measurement will require refinements to eliminate the divergence. In the study by Jorg Heland and Klaus Schafer [27], an aircraft exhaust plume was examined with FTIR emission spectroscopy. The experiment consisted of ground measurements with different types of engines and analyses with line-by-line software. The used K300 spectrometer was an industrial double pendulum Michelson interferometer that works with maximum non-iodized resolutions of 0.06 cm^{-1} between wavenumbers from 700 to 4000 cm^{-1}. In the first set of experiments, the old military M701-TZ engine was used, CO emission measurements were made at different thrust levels, and by changing the position of the camera downstream of the nozzle outlet, as shown in Figure 4. This study aimed to verify that the emission measurement equipment could work in difficult conditions. Results show typical accuracy of ±30% for CO_2, H_2O, CO, and NO emissions and in temperature results. Finally, to validate the measurements, an experiment was studied using a burner powered with propane gas, where the typical temperature reached by the exhaust gases is 400 °C. To be able to compare the tests with those carried out with standard equipment, NO and CO were entered. The CO and NOx results were satisfactory and showed an accuracy of ±20%.

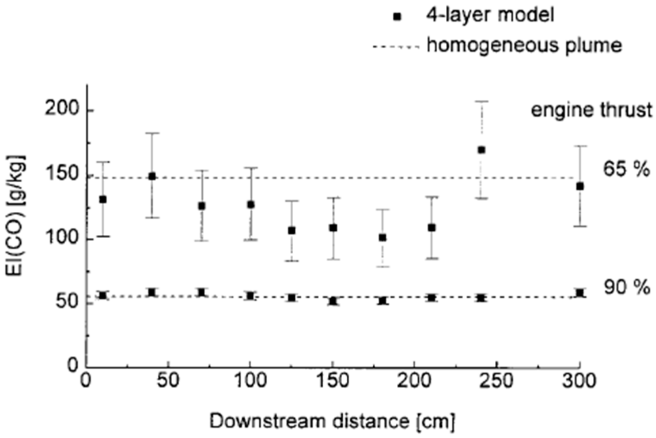

Figure 4. CO emissions at two different thrust levels for the engine ~65% and 90% taken at different locations downstream of the M701TZ engine. Reprinted with permission from Ref. [27] (1997).

The "overview to the ESA-EMAP project: characterization of SRM plumes with alumina particulate in subscale testing" of Saile et al. [28] deals with the experimental study of alumina particulates in solid rocket engines. In this work, the focus is on those particles that remain in the atmosphere after a solid rocket vehicle has passed. Fourier transform-based emission spectroscopy (FTIR) was performed with an ABB MR 304 spectroscope, which works between 1 and 8 µm and provided the results shown in Figure 5. In conclusion, spectroscopy allows one to precisely define the intensity as a function of the wavelength, and it provided the results in the study of the temperature of gases and particles.

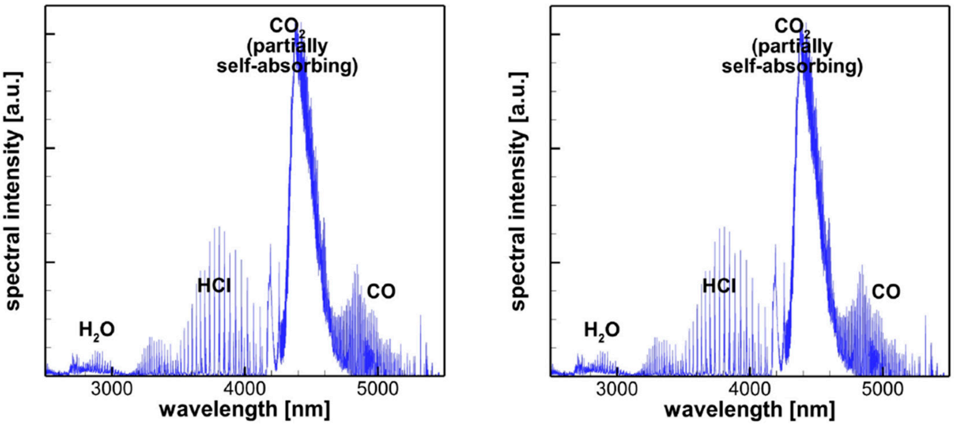

Figure 5. Relation between spectral intensity and wavelength of the rocket exhaust plume (Run031-V06-End). Reprinted with permission from Ref. [28] (2021).

In [29], radiometric FTIR was used to validate the implemented numerical model and to study rocket plumes, Mach numbers and rocket engine sizes at different altitudes for engines using HTPB and NEPE propellants.

It has been shown that the decrease in radiance with increasing altitude does not depend on whether or not afterburning is present. On the contrary, it has been verified that the total intensity varies with altitude and that this relationship also depends on the afterburning on the radiant area. The Mach number is inversely proportional to the total radiance to the total intensity and to the radiant area. Increasing the size of the engine results in both propellants increasing the altitude effect and decreasing the Mach number effect.

Devir [30] applied an FT-IR spectrometer to characterize the irradiance of a small solid fuel engine. Wang [31] used the FTIR method to characterize the infrared radiation signature of the exhaust gases of a solid rocket engine with three different propellant types, all with the double base but with different energetic characteristics. The infrared spectral radiance was measured in the range between 1000 and 4500 cm^{-1}. The results demonstrated that the energetic characteristics of the propellants affect the infrared radiation of the plume. FT-IR spectrometer measurements were also used to validate the numerical model.

3.2. UV–VIS Spectroscopy

Ultraviolet–visible range (UV–VIS) spectroscopy has the same main components as FTIR spectroscopy; the difference lies in the replacement of the interferometer with the monochromator. The monochromator is an optical system used to disperse polychromatic light that derives from the light source in monochromatic bands; each band is sent in succession on the sample.

There are two types of monochromators:

- based on filters, which block part of the light and allow to pass only a band;
- based on a dispersing element, which separates the various components of the radiation and allows the selection of the band.

UV (ultraviolet) spectrophotometers have been used together with FTIR spectroscopy in the study [26] to observe the optical emission spectra of gases (CO_2 and H_2O) and the broadband radiation that was measured by two Spectraline ES100 devices made by En'Urga Inc. (see Figure 6). Positioned orthogonally to each other and in the center of their view, the exhaust gases were positioned. The results show that the gas temperatures exceeded 2500 K, and those of the soot were approximately 1800 K.

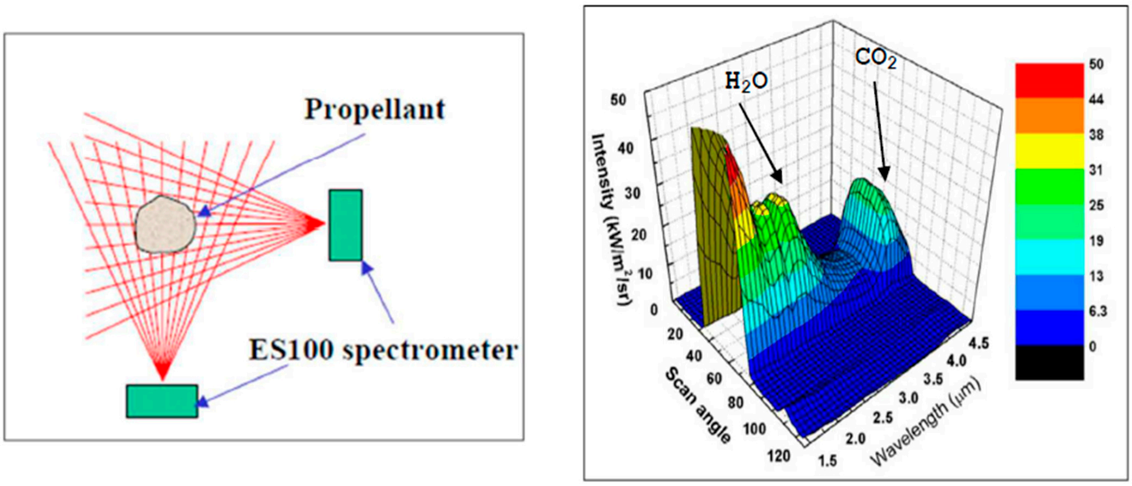

(**a**) (**b**)

Figure 6. (**a**) Setup for measuring CO_2 and H_2O gas. (**b**) Intensity spectrum obtained with the Spectraline system. Reprinted with permission from Ref. [26] (2014).

In the study by Hudson et al. [32], a laboratory-scale investigation of the spectral emissions of a hybrid rocket engine system was carried out. The exhaust emissions were investigated, and the results showed that the use of phenolic silica insulators led to base emissions consisting of the Na and K spectral lines and the C_2, OH, and CH combustion bands. The second part of the study investigated hydroxyl-terminated polybutadiene (HTPB), metallic emitting elements such as manganese, nickel, cobalt, copper, and iron that were added in the plume. A study on the effect of additive concentration was carried out only for manganese; the results showed that the emission spectra had a linear output in the range from 5 to 40 ppm. Overall, with the laboratory scale hybrid motor, plume spectroscopy can be easily used; therefore, it can be used to characterize the hybrid motor and solid rocket motors. Another work in which FTIR spectroscopy was used in conjunction with UV–VIS emission spectroscopy was the work of Saile et al. [28]. The Ocean Optics USB2000 spectrometer working in a spectral range of 200–850 nm was used for UV–VIS spectroscopy. The particle phase of the gray body radiation and the atomic lines of sodium and potassium are visible in Figure 7a.

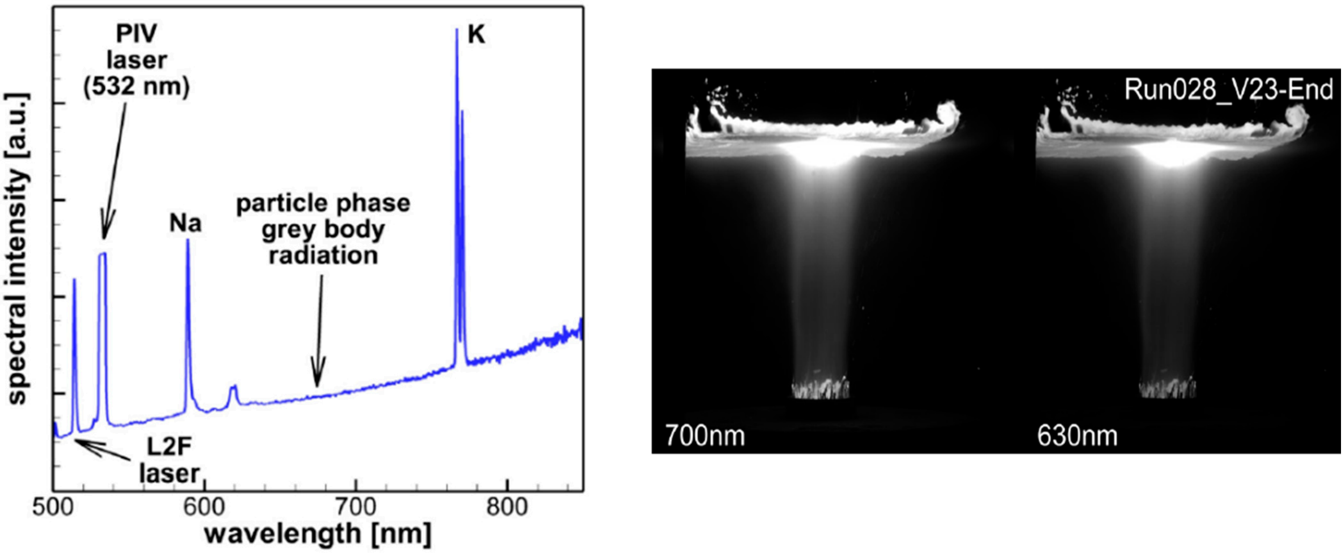

(**a**) (**b**)

Figure 7. (**a**) UV–VIS spectral intensity of the exhausted gases (5% aluminum, Run012-V29-End). (**b**) Images of the case with 18% of aluminum at 630 and 700 nm (Run028-23-End). Reprinted with permission from Ref. [28] (2021).

3.3. Alumina Emission Measurement (AEM)

Alumina emission measurement (AEM) was introduced by Saile et al. [32]. The purpose of this spectroscopic method is to provide information on the various species present in the plume. The idea of alumina emission measurements is to use the thermal emission of the alumina within the plume to determine its physical state. The AEM is effectively a two-color position resolution pyrometer. Two cameras take pictures at 630 and 700 nm, separately. A 650 nm dichroic mirror divides the light beam into two signals, which are then processed by 10 nm FWHM band-pass filters. The results provide the temperature and particle density derived from the intensity ratio of two synchronized images, as shown in Figure 7b.

4. Imaging IR

While with a normal camera, an image using visible light is acquired, with an infrared camera or thermal imager, an image using infrared (IR) radiation is recorded. Instead of the visible light camera's 400–700 nanometer (nm) range, infrared cameras are sensitive to wavelengths from about 1 to 14 µm beyond the visible spectrum. Therefore, with an infrared camera, it is possible to obtain highly detailed video or images that are not visible without any device. The IR camera is useful to characterize the exhaust plume of the rocket motor that presents large emissivity values in IR spectrum. The infrared cameras provide images of the plume that reveal features such as plume structure, turbulent flow, and shock diamonds. The irradiance signatures of the plume can be affected by several reasons, such as operating conditions of the motor, propellant components, and motor type. The solid rocket propellant often contains additives such as aluminum; thus, it is interesting to analyze the IR images of the plume of a solid rocket engine and to study the change in the structure of the plume and the variation of its characteristics as the amount of aluminum in the propellant. As already explained, the aluminum particles in the plume react with the particles in the atmosphere and produce alumina. Alumina is highly reflective and has a lower emissivity, and therefore has low transmission in the infrared wavelengths.

In previous studies, thermography was used to obtain the IR image of the plume to validate or improve numerical models and to find the correlation between the size or shape of the plume, and the results were obtained with numerical procedures. Devir, along with Avital et al. ([30,33]), analyzed the infrared signature for a ballistic engine (BEM) without metal elements in the propellant. The RADIANCE-1, a thermal imaging camera (Amber Engineering Inc., Goleta, California, USA) with a narrow IR filter to narrow the spectral range was placed at 9.4 m from the plume to obtain IR images of the plume.

In the article by Avital et al. [33], two different types of Ballistic Motor were analyzed; these motors differ in the expansion cone of the nozzle. The BEM-2 was lengthened to allow better observation of the exit plume, adjacent to the nozzle exit. The images were taken during the execution of a single test, thus in one motor firing. The time interval between consequent images was 0.5 s for BEM-1 and 1 s for BEM-2. The bandpass filters used with the camera pass frequencies were within 4.527–4.61 µm for the BEM-1 exhaust gases and within 4.372–4.516 µm for the BEM-2 exhaust gases. In the study, there was a comparison of the IR image obtained with the numerical simulation with the image provided by the thermal imager to verify the numerical model. The results showed good agreement between the numerically predicted BEM plume image and the experimental plume image. Therefore, it has been demonstrated that numerical simulations accurately describe the features of the plume. The results show better agreement between the IR image of the plume in the near field, namely at a small distance downstream of the nozzle outlet. The experiments of Avital [33] were also used for the validation of the numerical model in several studies [30,34]. The study by Qinglin NIU et al. [30] provided flow field properties by solving the axisymmetric Navier–Stokes equations with a finite volume technique. Therefore, the line of sight (LOS) method with Curtis–Godson approximation allowed us to obtain the spectrum. Figure 8 shows the comparison between the experimental radiation and that calculated analytically with a scan bandpass filter of 4.372–4.516 µm. The images are in good agreement; both the distribution of the "diamond" figures and the irradiance are comparable. An infrared thermal camera was also used for the analysis of the plume in the work of Robert P. Moran et al. [35]. The goal of the work was mainly the acquisition of acoustic and pressure data of the Ares I reusable solid rocket motor vehicle during the acoustic tests, a series of 18 static firing of solid rocket engines. The testing also incorporated a sound suppression system that used water. The inclusion of IR cameras during the tests was due to acquiring images of the plume structure, turbulent flow, and shock diamonds.

The infrared images are shown in Figure 9 and clearly illustrate shock diamonds that could not be captured in the visible wavelengths. Infrared images were acquired using the FLIR T400 IR camera during the rocket test to support the verification or enhancement of numerical models and to verify the effects of the noise-suppressing water system on the size and shape of the rocket plume. One test was conducted without water, and the other test was conducted with water; the environment in the second test was more challenging due to water and water droplets that hindered the heat transmission; therefore, the plume structure results are clearer in the image without water.

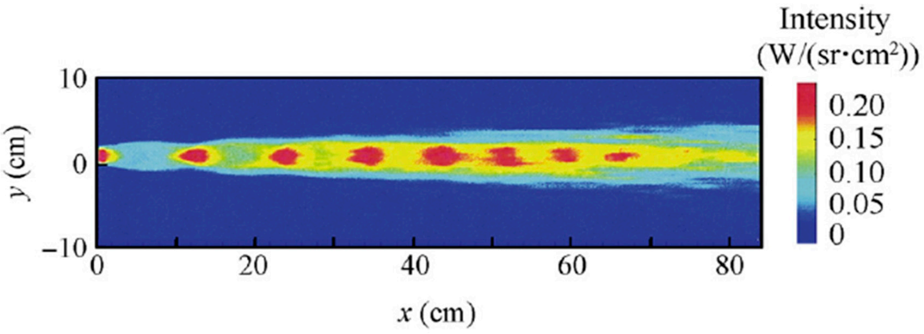

(a) Experimental IR image [7]

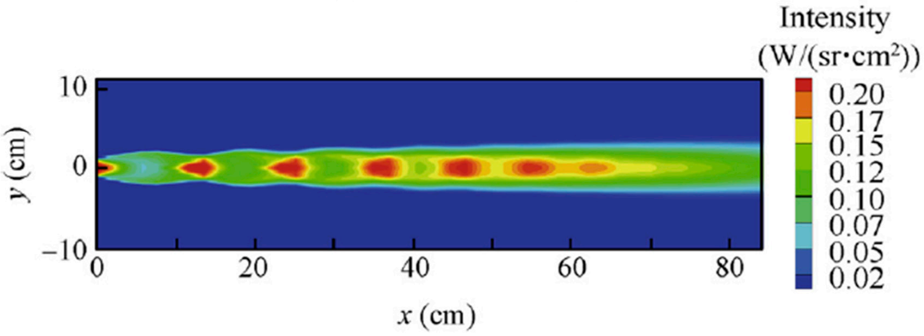

(b) Calculated IR contour

Figure 8. Comparison of experimental and calculated infrared images of the plume by Avital et al. [33] with the scan bandpass filter of 4.372–4.516 µm. Reprinted with permission from Ref. [30] (2017).

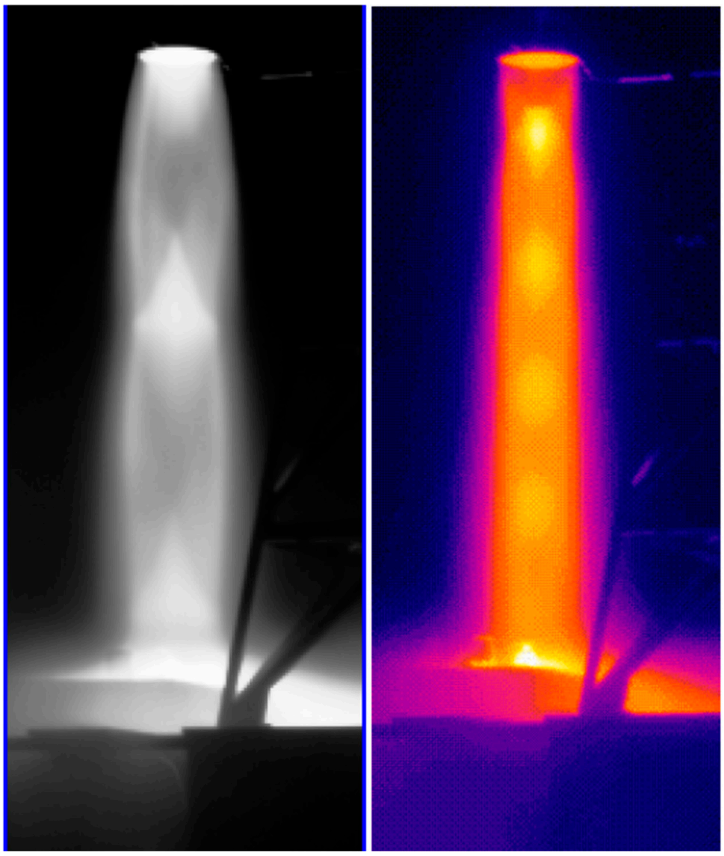

Figure 9. Infrared images were obtained with SC655 IR Camera taken during an Ares I test in the lift-off condition. Reprinted with permission from Ref. [30] (2011).

5. Shadowgraph Technique

Schlieren and shadowgraph have been implemented since the 17th century [36] and have been greatly used for seeing the invisible by using "white" light for imaging during wind tunnel testing and characterization of high-speed flows as rocket plume. These optical techniques use lenses, mirrors, and cameras to determine refractive noise in transparent media.

The shadowgraph technique is based on the detection and characterization of the shadow created on the visualization screen, due to the density of the fluid under observation. The shadowgraph generated on the screen is related to the second derivative of the refraction index of the fluid media in the space.

The darker region (the shadow) is in the place corresponding to the denser region: the light passing between the ambient air and the denser region is deviated by an angle related to the refraction index, according to the Snell law (Figure 10).

The deviated light beam does not hit the screen directly, but at another point, making the points beyond the denser region darker and the points beyond the less dense region brighter (Figure 11).

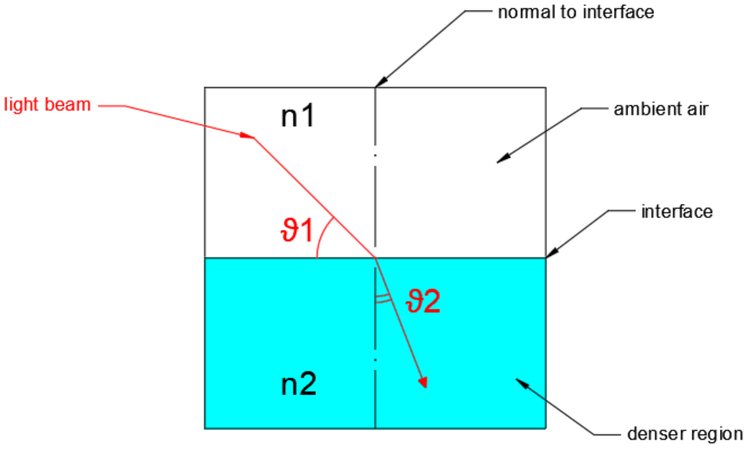

Figure 10. Snell law.

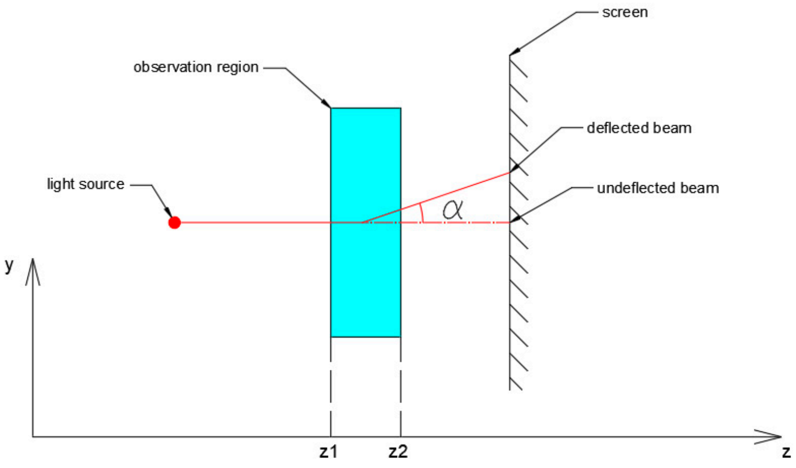

Figure 11. Shadowgraph principle.

$$n1\sin(\vartheta 1) = n2\ \sin(\vartheta 2) \tag{9}$$

The numeric parameter of this phenomenon is the contrast $\frac{\Delta I(x,y)}{I(x,y)}$, where I is the light intensity, and <*xy*> is the plane where the shadow effect is observed with its reference system (considering z the direction of the light beam) [37]. The contrast concerns the Laplacian of the refraction index.

Due to the simplicity of the phenomenon, the basic layout is easy: only a source light, a white screen, and gradient of density (due, in the cases discussed in this document, to the compressible flow effects) are needed for the basic observation.

In everyday life, the shadowgraph effect can be experienced when a liquid evaporates close to a white wall on a sunny day: the shadow created by the vapor can be visualized on the wall; thus, to visualize the phenomenon, no particular instrumentation is needed. In the aerospace field, the refraction of light can be easily experienced during take-off, close to the engines, where both compressible and thermal effects create a density gradient that deviates the light rays coming from the background.

In the laboratory scale, it is necessary to optimize the visualization. With this aim, a point light source with a collimating lens basically can be used that makes the light beams parallel to each other, as shown in Figure 12.

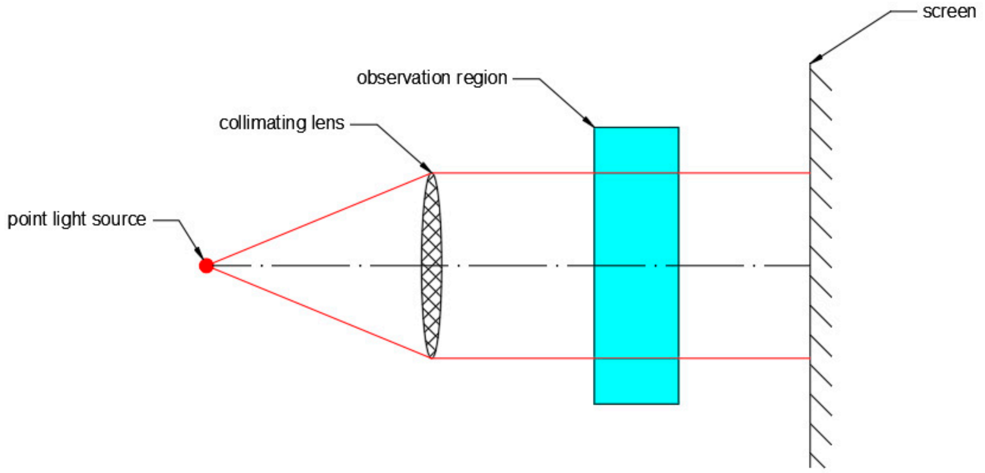

Figure 12. Basic shadowgraph layout.

The next target is to record the phenomenon with different scales. This is made using a camera as the visualization screen and a lens system (the objective); see Figure 13.

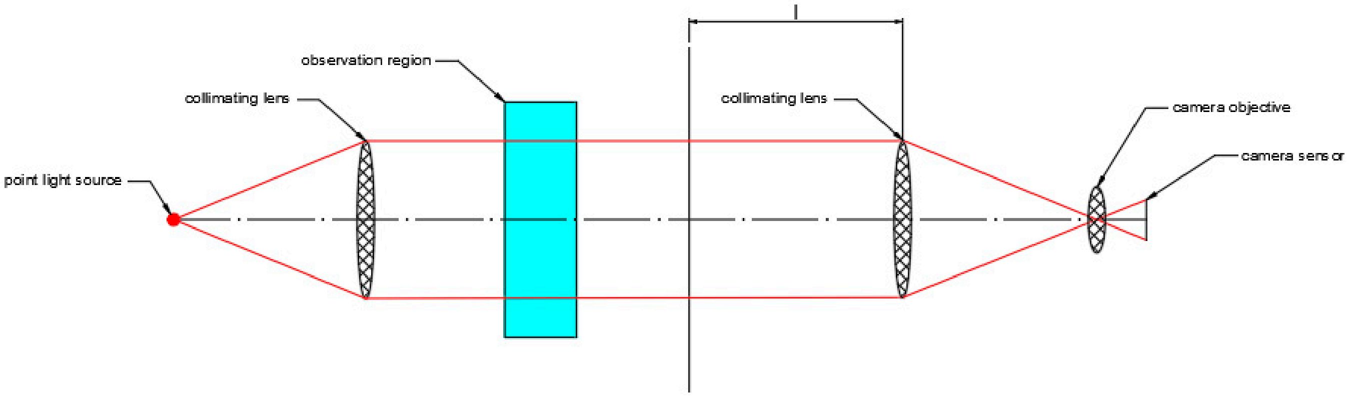

Figure 13. Basic shadowgraph layout with camera.

The distance l between the observation region and the visualization screen is important for the value of the contrast: it depends also on the Laplacian of the refraction index in the plane parallel to the plane of observation, through [37]:

$$\frac{\Delta I(x,y)}{I} = l \int_{z1}^{z2} \left(\frac{\partial^2}{\partial x^2} + \frac{\partial^2}{\partial y^2} \right) \ln[n(x,y,z)]dz \tag{10}$$

In the aerospace applications, in which many phenomena to be observed are characterized only by compressible effects with little changes in the refraction index, a double-pass configuration with a retroreflective screen is implemented to improve the sensitivity to low-density variation. This layout is called retroreflective shadowgraph [38]; see Figure 14. In this case, the beam splitter points the image directly on the camera, using an "on-axis" layout, it permits one to avoid doubling some regions of the image due to the angle of the axis of the illuminating light with the axis of the camera.

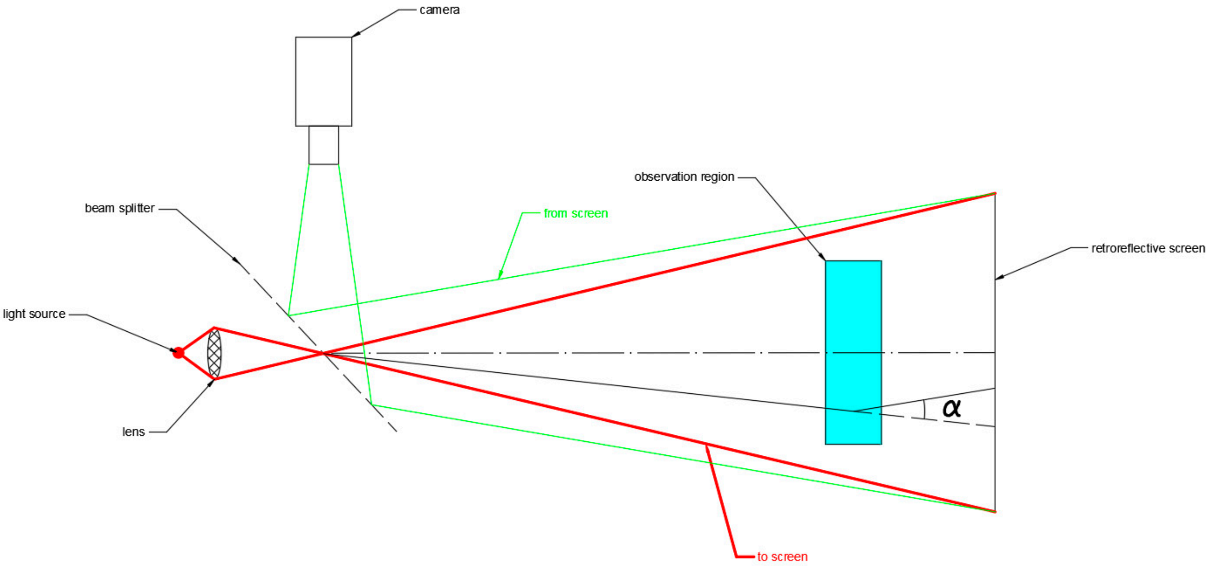

Figure 14. Retroreflective shadowgraph layout.

Because not a particular screen is asked to visualize the shadows, changing the retroreflective screen with a spherical mirror makes it possible to visualize the circular section of the conical light ray coming back from the mirror.

This last configuration has been used to visualize the flow out of a supersonic nozzle at 6 bar in the Green Engine Lab at the University of Salento using the Imperx B2020M camera. Figure 15 shows that this technique makes possible the visualization of all the flow structures.

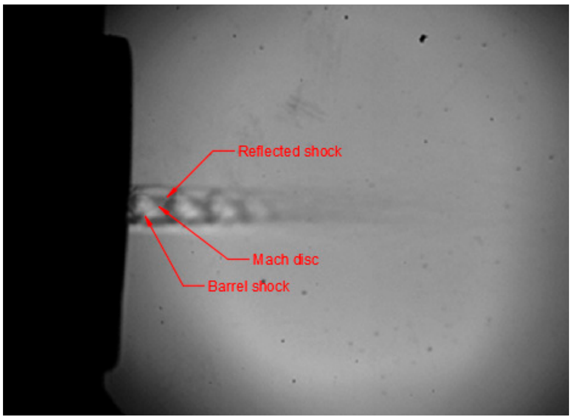

Figure 15. Shadowgraph of a supersonic nozzle taken with a Imperx B2020M camera, and an exposure time of 0.5 ms.

As an example of shadowgraph applied for the characterization of rocket plumes, Figure 16 shows a Mach shock cell of the experimental shadowgraphs used to validate analytical methods for simulating inclined impinging exhaust jet from a rocket engine.

Flow fields resulting from the under-expanded jet that hits the plate were compared with the experimental results at different impact points on the plate (h), impinging angle (θ) and the ratio between the nozzle outlet pressure and ambient pressure, NPR [39].

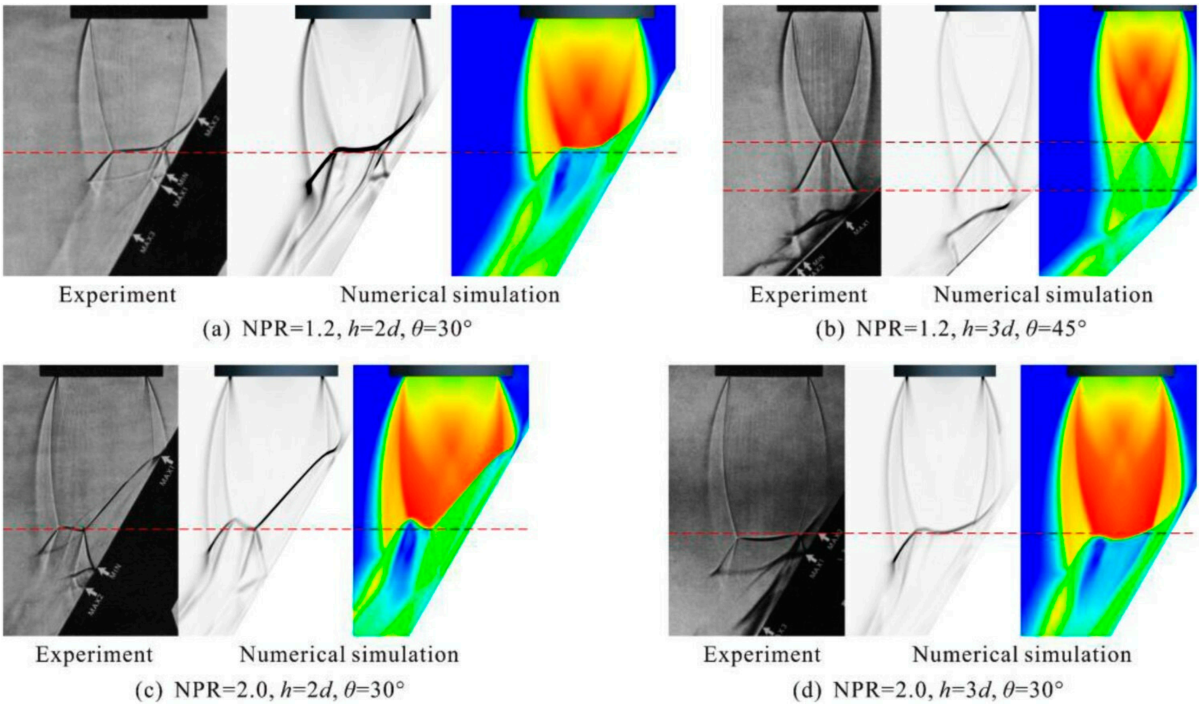

Figure 16. Experimental shadowgraph results and numerical simulation results for an inclined impinging jet with different geometrical parameters. Reprinted with permission from Ref. [39] (2022).

6. Schlieren Technique

The Schlieren technique is more sensitive to the gradient of density (the first derivative, instead of the shadowgraph being related to the second derivative). Both techniques were thought up by Hooke around 1665 in [40], but the first to use it in a scientific work was Toepler [41], with the layout in Figure 17, where the Schlieren head could be a convergent lens or a spherical mirror. The fundamental differences that make the technique more sensitive are the requirement for the light source to be a point and the introduction of the knife-edge. This increases the contrast in the image, cutting off part of the light deflected by the fluid media observed once the light is made into a circle (the normal section of the conical light ray).

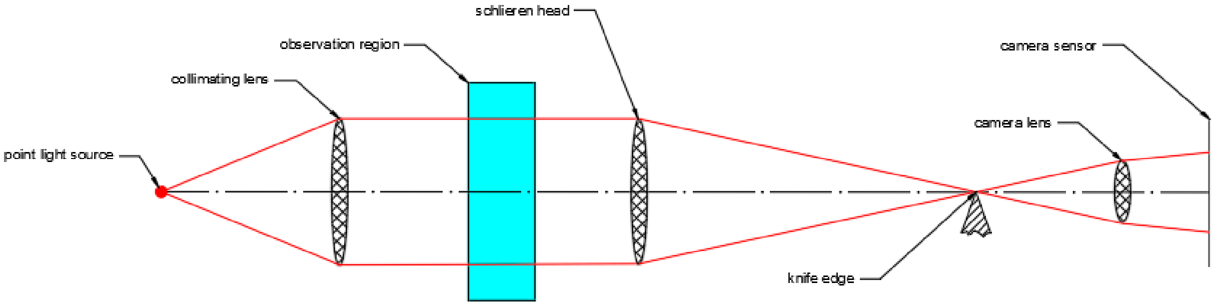

Figure 17. Basic Schlieren layout with camera.

Considering a deflection of the light in the y direction (of an angle ε_y), using the notation in Figure 18, the contrast could be calculated as [37]

$$\frac{\Delta I}{I} = \frac{\Delta a}{a} = \frac{f}{a}\tan\varepsilon_y \tag{11}$$

with f the focal length of the Schlieren head; thus,

$$\frac{\Delta I(x,y)}{I} = \frac{f}{a}\int_{z1}^{z2}\frac{1}{n}\frac{\partial n}{\partial y}dz \tag{12}$$

and for a gas flow

$$\frac{\Delta I(x,y)}{I} = \frac{Kf}{a}\int_{z1}^{z2}\frac{\partial \rho}{\partial y}dz \tag{13}$$

where K is the Gradstone–Dale constant.

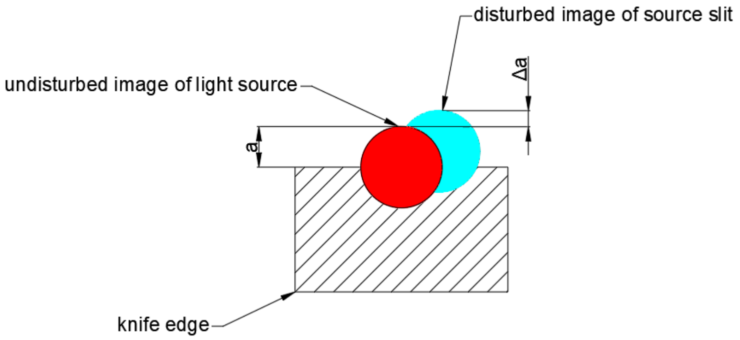

Figure 18. Knife edge working principle.

Different layouts for this technique have been developed in the aerospace field, as well as for the Schlieren and for the shadowgraph. One of the most used layouts is the double-pass configuration, in which, to increase the sensitivity to small changes in density, a conical light beam passes twice through the test field; see Figure 19.

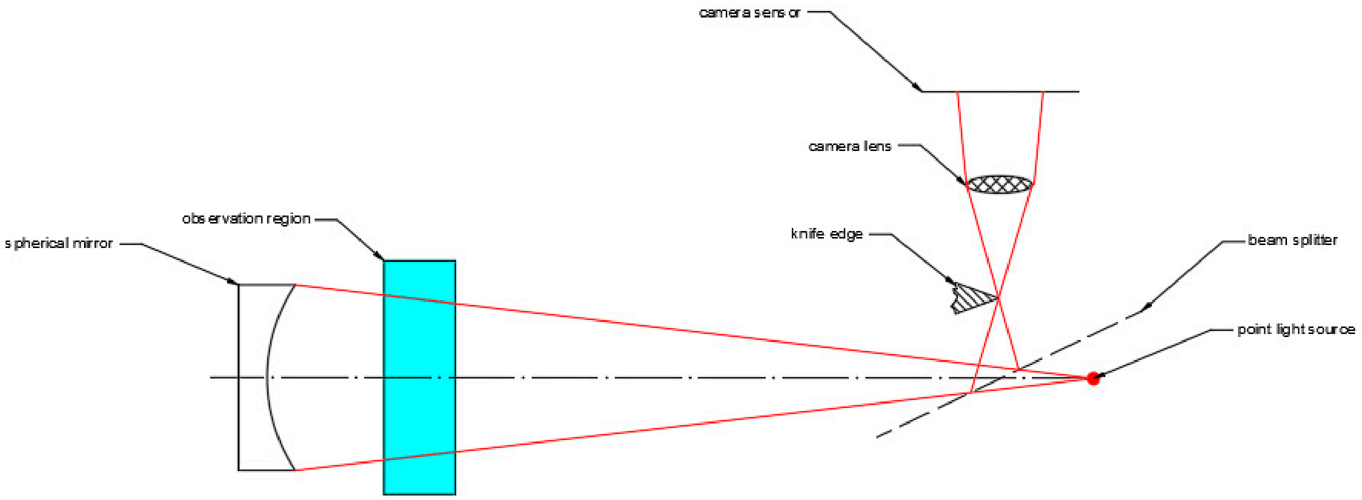

Figure 19. On-axis double-pass Schlieren layout.

It is obtained using a spherical mirror as the Schlieren head. The rays reflected by the mirror converge on the focal point and make a spot in the center of the sphere. Positioning the point light source in the center of the sphere, the reflected spot is exactly in the same point, such that all the rays hitting the mirror pass twice through the flow field.

This perfect alignment permits us to see the shadowgraph, without doubling the image, in all the circular sections of the cone; thus, using the beam splitter, we can see the same section in the camera. The knife-edge lets us increase the contrast, as shown in the previous calculation.

Relevant work in the characterization of the SRM plume through Schlieren has been developed in [42], to visualize the flame structure, flame propagation and to track solid particles in the plume due to the combustion of propellant composites, in which the presence of perchlorate ammonium (AP), hydroxyl-terminated polybutadiene binder (HTPB) and metal loads such as aluminum particles leads to the expulsion of solid particles, mainly alumina.

The size range covered by solid-phase in SRM (solid rocket motor) could be wide, from a few micrometers for the fine AP or/and additive charges to a few hundred micrometers for coarse AP grains.

The flame structure was visualized with the FST layout (focusing Schlieren technique), reported in Figure 20, to compare the experimental results with numerical simulations (species concentration, temperature, etc.). A focusing Schlieren system involves the same basic components as conventional Schlieren, i.e., a light source, an imaging lens, a cut-off, and an image screen. The difference is to use a matrix of slit light sources instead of a single slit light source. These light sources are displayed through a lens on a grid, which acts as a cut-off.

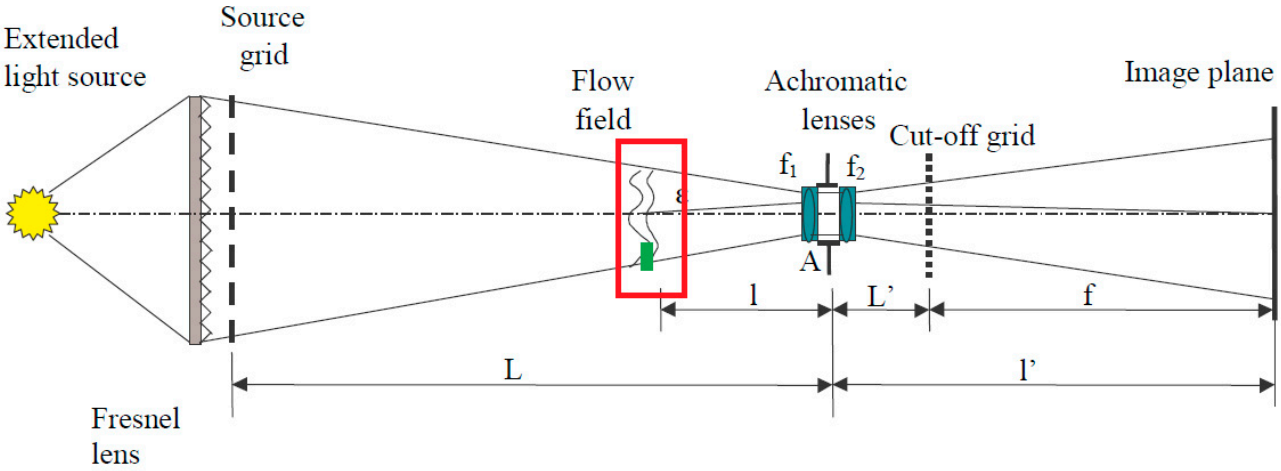

Figure 20. Focusing Schlieren technique layout. Reprinted with permission from Ref. [42] (2011).

Figure 21 shows the results obtained with this layout in the visualization of the flame structure of HTPB/AP/HTPB sandwiches [42]. An advantage of these techniques is related to not being affected by the light emitted by the phenomenon observed. This allows the authors to investigate the ignition and the flame propagation of an aluminized propellant, fired up by a CO_2 laser beam, as shown in Figure 22, where the ignition phase and fame propagation by shadowgraph can be observed. When the beam hits the surface, a gradient of density is generated due to the hitting, thus leading to the ignition and flame propagation stages, in particular the ignition between instant 5 and 7, while the time steps after 7 are related to flame propagation. The visualization of particles ejected in the plume from a composite propellant ((60 + 6)% of AP, 16% of HTPB, and 18% of Al (30 μm)) was based through a little field of view 2.72 × 1.36 mm2 (1024 × 512 pixels), and a resolution of 1024 × 512 pixels, with a correlation factor of 2.65 μm/pixel, where the raw images acquired in the Schlieren setup are compared with the post-processed images (see Figures 23 and 24). In this work [42], the authors extract the particle from the "noise" of the images by subtraction of one image before ignition, being able to recognize a particle using at least 10 pixels. The experiments on the Ariane 5 composite propellant (multi-modal AP and 18% Al. 30 μm), with a field of view of 1 × 8 mm^2–128 × 1024 pixels and a frame rate of 15,000 f/s, gave the images in Figure 24.

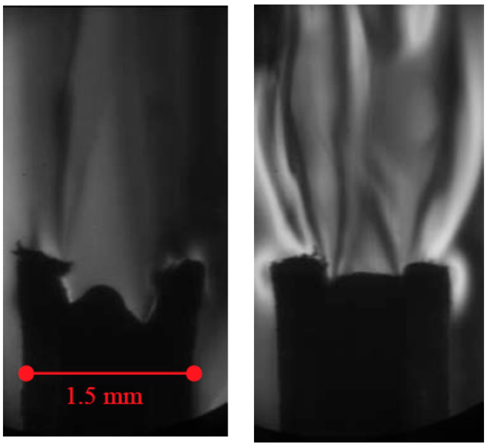

Figure 21. HTPB/AP/HTPB sandwiches at 0.5 MPa (**left**) and 1.5 MPa (**right**). Reprinted with permission from Ref. [42] (2022).

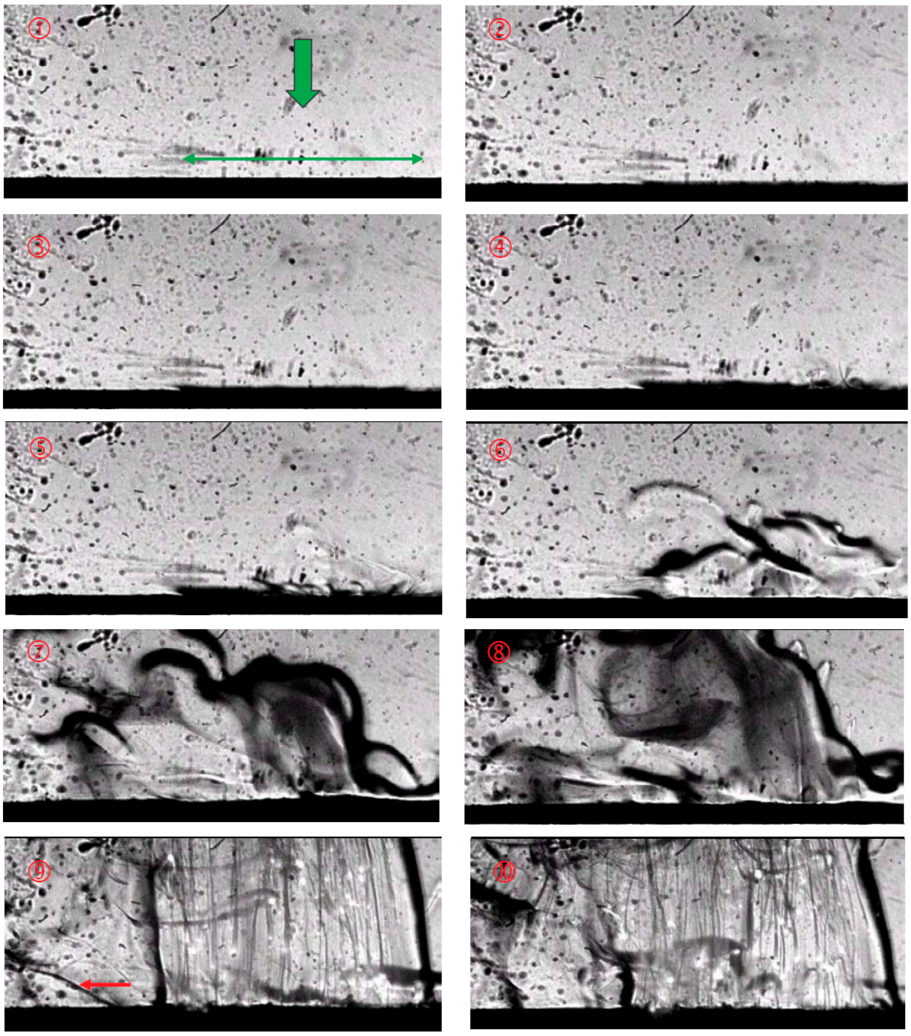

Figure 22. HTPB/AP/Al propellant ignition phase and fame propagation by shadowgraph, represented in subfigures from 1 to 10 with a time interval of 1 ms, where (1) is the ignition instant (with a CO_2 laser). Reprinted with permission from Ref. [42] (2022).

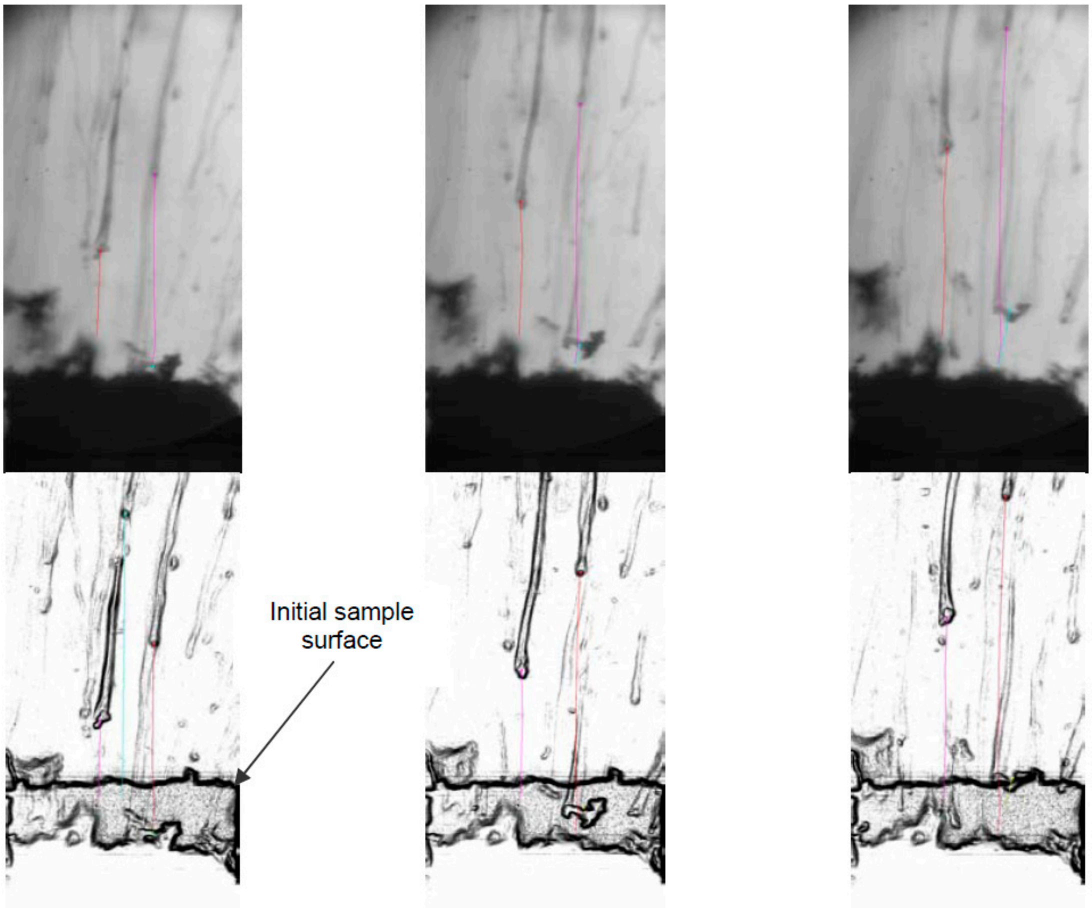

Figure 23. Particle tracking without and with FST: processing of acquired images (top) and post-processed images (bottom). Reprinted with permission from Ref. [42] (2022).

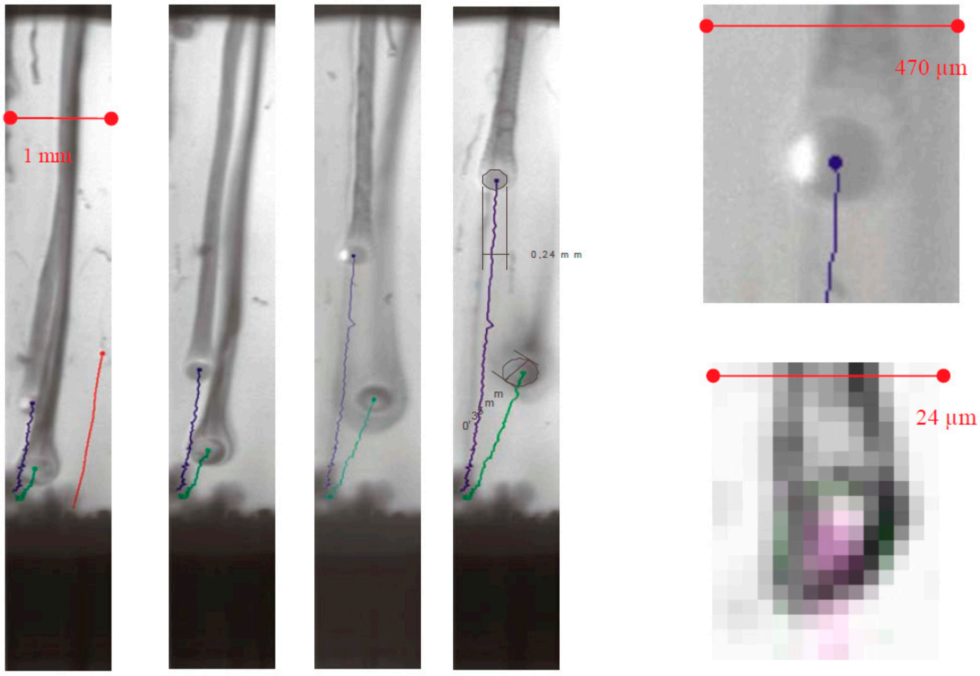

Figure 24. Alumina particles in composite propellant. Reprinted with permission from Ref. [42] (2022).

The high speed Schlieren technique is also used in work [43] during a cold-flow sub-scale nozzle campaign to visualize the flow structure at the exit of a supersonic overexpanded thrust-optimized parabolic (TOP) nozzle flow, where restricted shock separation (RSS) phenomena can lead to a side-load that is dangerous for launchers at sea level. The authors used the Schlieren to validate numerical data obtained in the development of a new shape for contouring the internal wall of the nozzle. Figure 25 shows the nozzle tested, and Figure 26 shows the Schlieren image of a TOP contoured nozzle, with an indication of the flow characteristics relevant to the author.

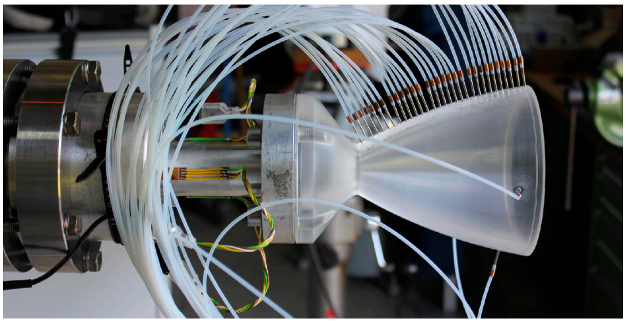

Figure 25. Experimental nozzle used in the experimental work. Reprinted with permission from Ref. [43] (2017).

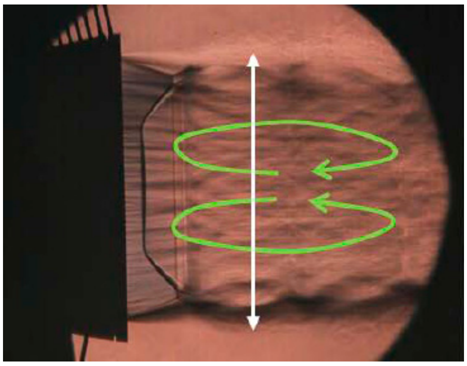

Figure 26. Flow features at a TOP contoured nozzle exit, viewed using Schlieren technique. Reprinted with permission from Ref. [43] (2017).

Basically, the shadowgraph and the Schlieren are qualitative techniques. One of the main issues in the application of these techniques is to make them more quantitative. Hence, the color Schlieren was implemented in the literature. The color Schlieren was experimented by Toepler [39], substituting the knife edge with color bands in a way that the deflected beam, instead of being cut by the knife edge, would be colored with two different colors, based on the sign of the density gradient (positive or negative). In Figure 27, an example of color Schlieren applied to a supersonic nozzle, for an air-to-air jet, is shown.

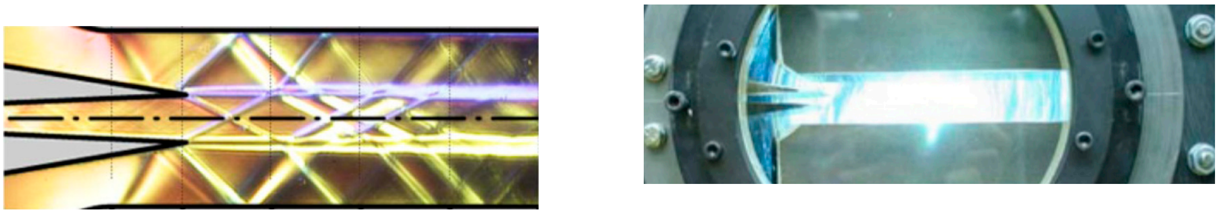

Figure 27. Example of color Schlieren out of supersonic nozzle in an air-to-air ejector (**left**), experimental apparatus (**right**). Reprinted with permission from Ref. [44] (2013).

In [45], rainbow Schlieren deflectometry was used with computed tomography to measure the three-dimensional density fields of free jets containing shock from micro nozzles. The layout of the laboratory set-up is shown in Figure 28, wherein the <*xz*> plane feeding system of the nozzle is well explained: an electrovalve regulates the flow going inside a plenum chamber, where the dynamical pressure effect is dumped. The digital thermometer and the pressure transducer let us know the stagnation state variable at the inlet of the nozzle.

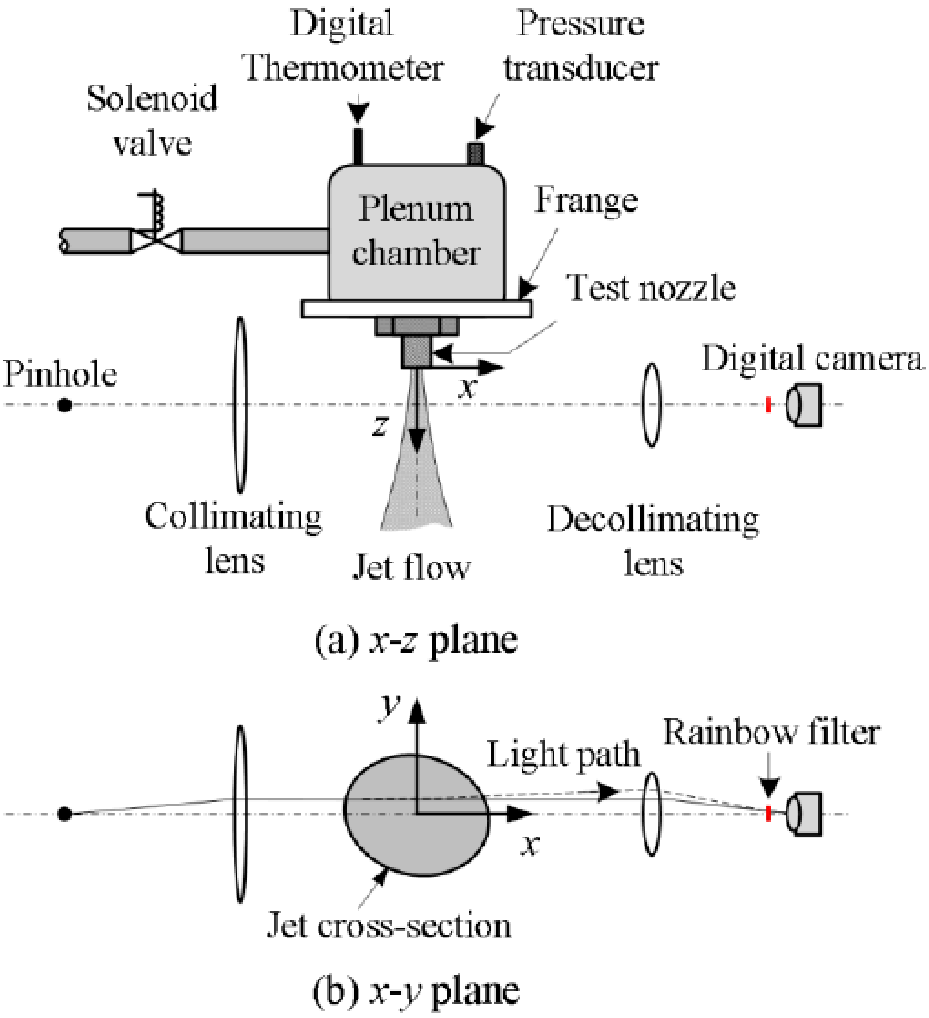

Figure 28. Experimental layout for rainbow Schlieren combined with computer tomography. Reprinted with permission from Ref. [45] (2018).

In the <*xy*> plane, instead, there is a description of the visualization system, where the flow section is centered in the reference system, and the light beam moves from left to right, passing through two lenses and the rainbow filter (Figure 29).

An important issue in the rainbow Schlieren is that the accuracy of the experimental system results depends on the size of the source image, the focal length of the collimating lens, and the resolution of color gradients on the rainbow filter (Figure 29). This technique requires the calibration of the system, moving the rainbow filter in the Schlieren cut of the plane and reporting the hue as a function of the coordinate of the filter (Figure 30).

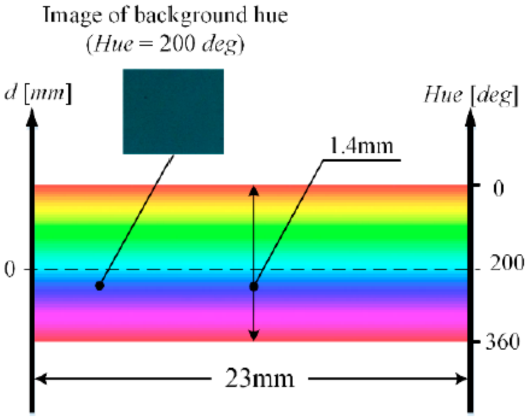

Figure 29. Rainbow filter with hue value. Reprinted with permission from Ref. [45] (2018).

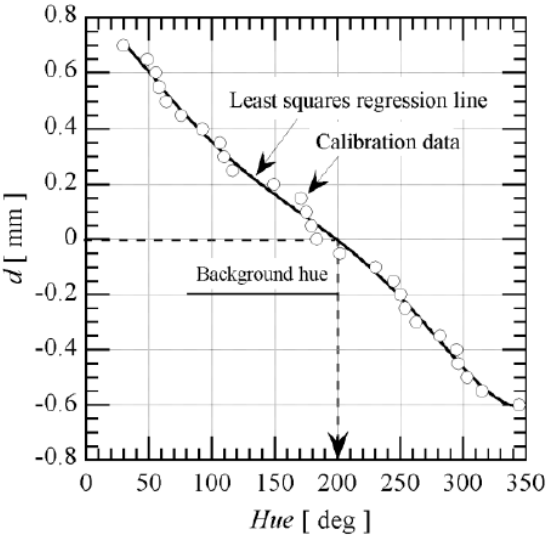

Figure 30. Calibration curve of the rainbow Schlieren system. Reprinted with permission from Ref. [45] (2018).

A 3D analysis [45] is performed at a different constant z coordinate, rotating the nozzle around the z axis, which was required because the nozzle was not axisymmetric. The images acquired with the rainbow Schlieren are less detailed (in terms of edges) than the other Schlieren techniques (Figure 31), and the key role is played by the post-processing with the convolution-back projection algorithm (CBP). As a result, this post-processing algorithm returns a contour plot with the values of the density field (Figure 32). This result is validated in the work with a theoretical expectation, demonstrating its value in the experimental studies (Figure 33).

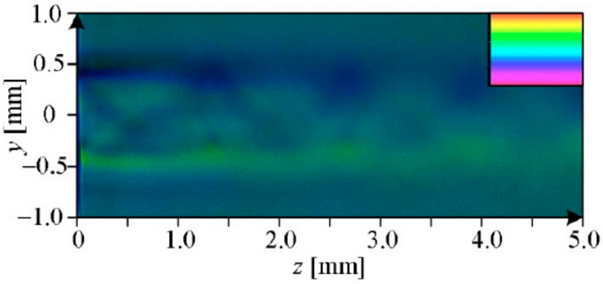

Figure 31. Rainbow Schlieren flow visualization. Reprinted with permission from Ref. [45] (2018).

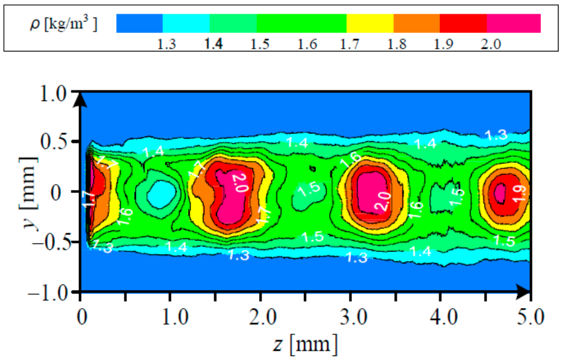

Figure 32. Rainbow Schlieren post-processing density contour plot. Reprinted with permission from Ref. [45] (2018).

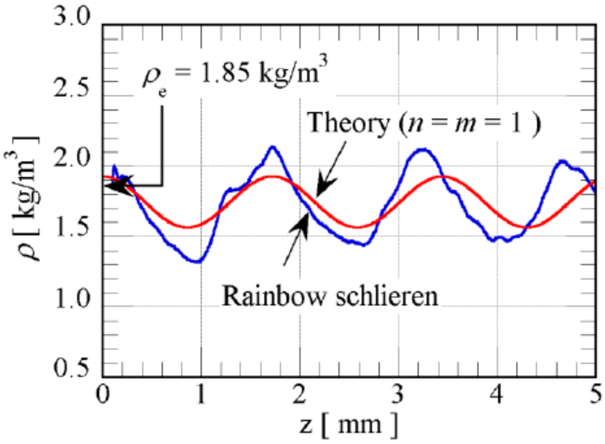

Figure 33. Theoretical/experimental data comparison for the rainbow Schlieren. Reprinted with permission from Ref. [45] (2018).

Background oriented Schlieren (BOS) is the digital version of Schlieren imaging. In the BOS layout, some random points are captured in the background of the flowfield with a high-resolution camera. The BOS technique evaluates the apparent displacement caused by the aero-optical effects of a dot pattern through a camera. The presence of an intermediate index gradient due to compressibility effects or hot flow is the cause of the aero-optic effects. The 3D density field will be estimated through the apparent displacement of the pattern and the light ray deviation maps that have been obtained from a given number of points of view.

At NASA's Glenn Research Centers Altitude Combustion Stand (ACS), many tests are carried out, implementing the background oriented Schlieren, BOS, the technique to visualize the plume of a small rocket engine under altitude testing conditions, using nitrogen as the exhaust gases simulant [46].

A new approach was taken using the background patterns provided by a 4K HD monitor that provided a self-illuminated speckled background, as shown in Figure 34. The BOS system is capable of detecting expansion fans due to low mass flow nozzles and near-vacuum conditions.

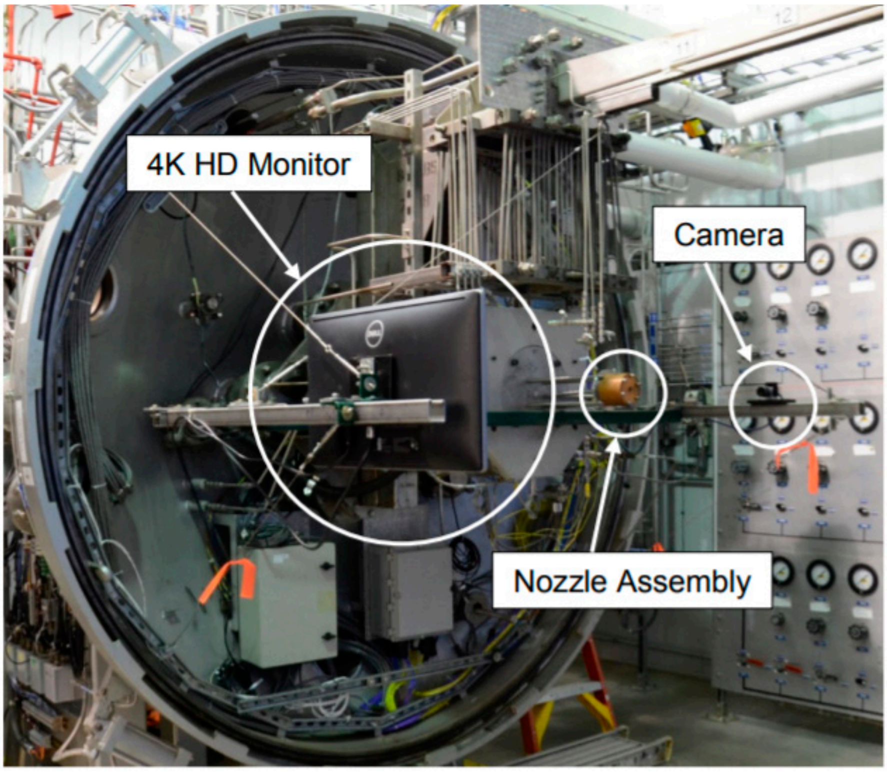

Figure 34. Theoretical/experimental data comparison for the rainbow Schlieren. Reprinted with permission from Ref. [46] (2017).

It has been shown that the accuracy of the results obtained with the BOS technique is affected by the difference between the test article and the speckled background pattern. In the case of a fixed camera, the only option to speckle the distance of the pattern is the reduction of the focal length of the lens that increases the FOV, but the resolution of the BOS results decreases. Each component of the density field derivative was integrated into both dimensions to obtain a reconstruction of the original density field, as shown in Figure 35.

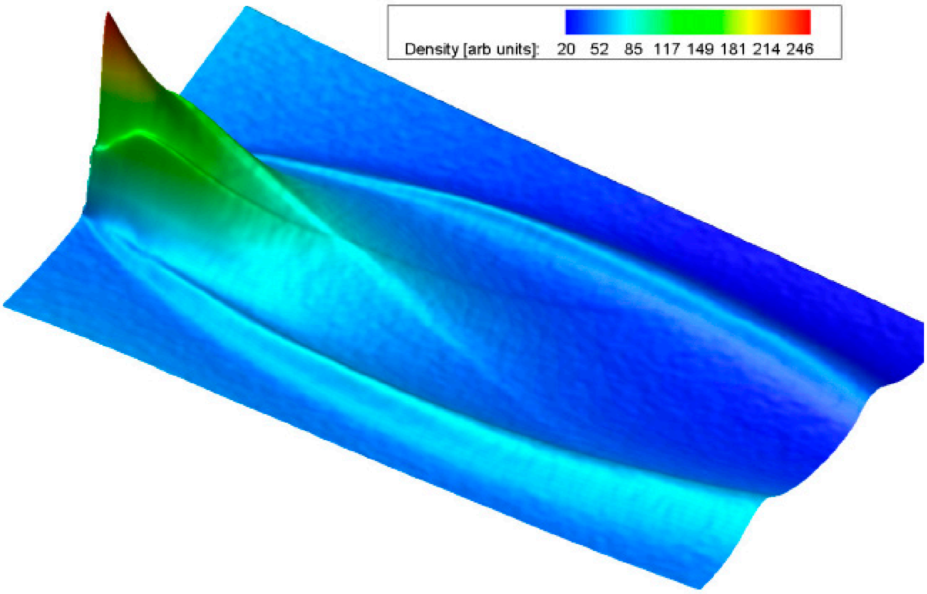

Figure 35. Theoretical/experimental data comparison for the rainbow Schlieren. Reprinted with permission from Ref. [46] (2017).

Schlieren image velocimetry (SIV) is a non-intrusive method obtained by the combination of Schlieren techniques and cross-correlation methods to give an estimation of flow velocity by tracking the motion of naturally occurring refractive turbulent eddies in a flow as virtual "seed particles" [47]. As particle image velocimetry (PIV), SIV estimates simultaneous velocity without the use of tracer particles. Schlieren images give a 2D path average of the fluid flow. The images should be pre-processed to improve the quality of the turbulent features and reduce the background noise. After that, cross-correlation methods are applied to obtain velocity measurements.

In [48], it was verified that the use of a pulsed light source with light-emitting diodes instead of twin pulsed lasers results in an important improvement in the velocimetry of the Schlieren image.

7. Digital Inline Holography (DIH)

The techniques discussed until now are based mainly on image acquisition and processing. In the traditional image acquisition, the relevant physical quantity recorded is the intensity of light. The holography that is based on the DIH allows the user to record both the phase and the amplitude of the front wave of light.

The technique allows the user to record more information than what can be recorded with the traditional image acquisition techniques: the word "holography" comes from Greek and means "writing all" the information about the light wave. The traditional image acquisition records only information about the intensity; instead, holography permits one to record information about the amplitude and the phase and to create a 3D visualization of the object through the interference pattern created by a coherent light (emitted by a laser) and split into two beams, one of which illuminates the object under investigation, while the other creates a reference. The holography aims to reconstruct the wavefront coming from the object under observation when the object is removed.

In optical holography, the interference pattern, when is illuminated only by the reference ray, reproduces the 3D image of the object: the setup with the object impresses on the recording medium the interference pattern, and when removing the object, the 3D image is reconstructed in the same position if the illuminating ray is the same as the reference ray, as shown in Figure 36.

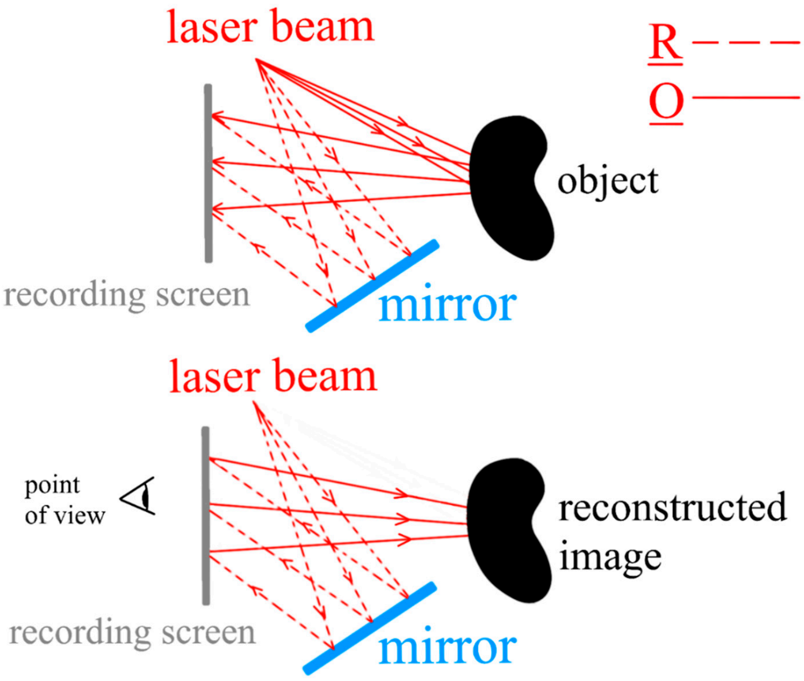

Figure 36. Holography working principle.

From the mathematical point of view, thinking to the wave nature of the light, we can model the coherent ray with a complex number: the wave with its amplitude and phase.

For the reference ray ($\underline{R}$), marked with *, the complex conjugate of the complex numbers:

$$\underline{R} = Re^{j\psi} \tag{14}$$

For the light coming from the object ($\underline{O}$), instead we have

$$\underline{O} = Oe^{j\varphi} \tag{15}$$

thus, the intensity of light (I) impressed on the recording medium is

$$I = |\underline{O} + \underline{R}|^2 = |\underline{O}|^2 + |\underline{R}|^2 + 2|\underline{O}||\underline{R}|\cos(\psi - \varphi) \tag{16}$$

The last equation reveals as the $2|\underline{O}||\underline{R}|\cos(\psi - \varphi)$ term contains information about the amplitude of the light coming from the object $|\underline{O}|$ and its phase φ, while the $|\underline{O}|^2 + |\underline{R}|^2$ is a DC term in the frequency domain.

In optical holography, the intensity of the interference pattern records the information about the amplitude of the light, and the position of the fringes records the information about the phase.

In digital holography, the recording screen is the camera sensor that could be a CCD or a CMOS, and the process to reconstruct the wavefront coming from the object has to be simulated, extracting the $|\underline{O}|$ and φ. The way this can happen depends on the arrangement of the holographic system.

In the applications shown below, the typical image acquired with haplographies and characterized by black and withe fringes are reported.

In [48], the authors studied the burning surface of sticks containing alumina powder, with the aim to characterize the alumina particulate shown in Figure 37. Figure 38 shows the hologram, characterized by its fringes.

In particular, the setup used to record the holograms is shown in Figure 39, where the laser beam is open in a cylinder of light with a diameter coherent with the ROI, and the hologram is recorded by the optical system "Holography Camera and Lens".

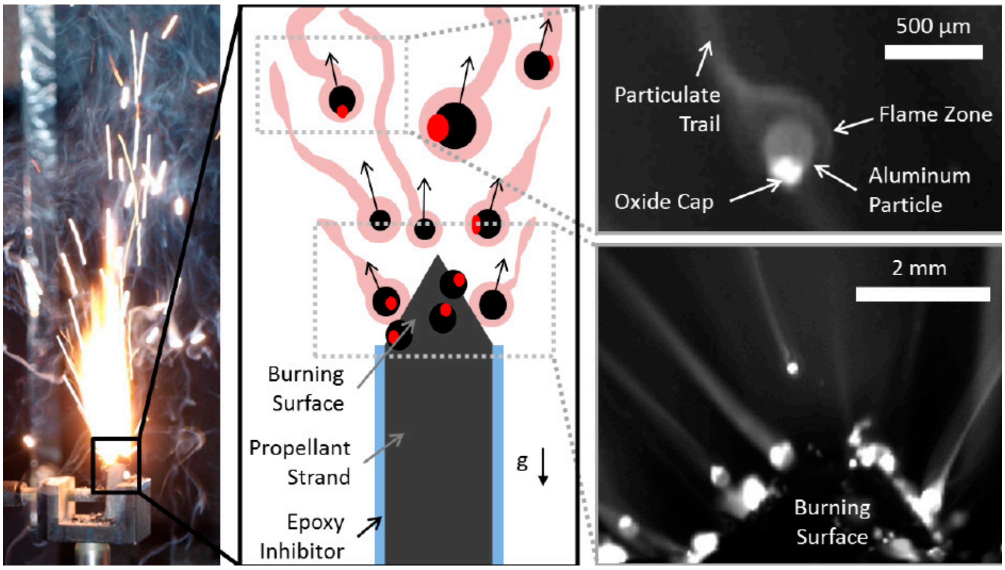

Figure 37. Stick's burning surface. Reprinted with permission from Ref. [49] (2017).

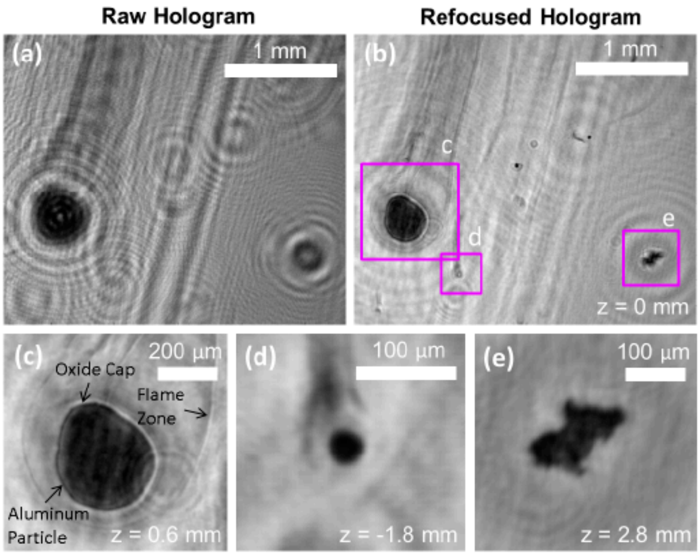

Figure 38. Alumina hologram, (**a**) Raw Hologram; (**b**) Refocused Hologram at z = 0; (**c**–**e**) are refocused holograms with different z values (depth of the recorded volume), to focus on specific particles. Reprinted with permission from Ref. [48] (2017).

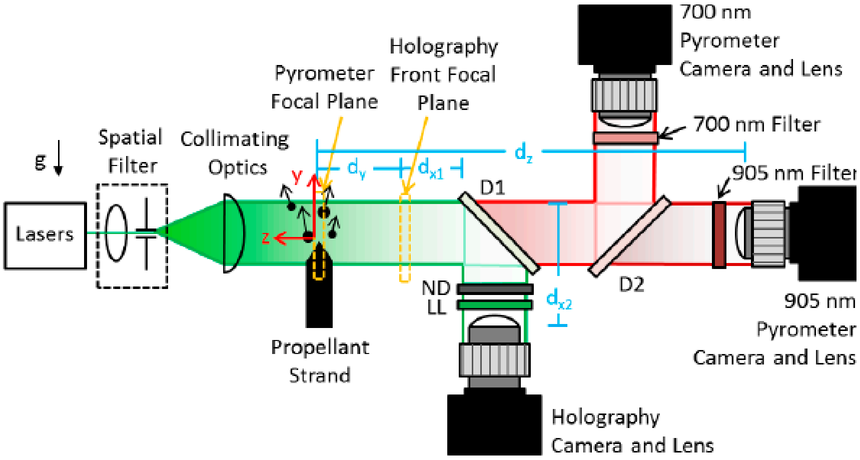

Figure 39. Setup for combined DIH and pyrography. Reprinted with permission from Ref. [48] (2017).

The experimental apparatus related to DIH consists of:

- Laser: Continuum MiniLite PIV ND:YAG lasers (532 nm, 5 ns pulse duration);
- ND: Neutral Density filter;
- LL: Laserline filter at 532 nm with a bandwidth of 1 nm (Andover 532FS02-50);
- Camera objective: Infinity K2 DistaMax long-distance microscope;
- Camera: LaVision sCMOS monochrome camera (2560 × 2160 pixels, 6.5 µm pixel pitch, 16 bit depth)

8. Tuneable Diode Laser Absorption Spectroscopy (TDLAS)

Tuneable diode laser absorption spectroscopy (TDLAS) is a contactless non-intrusive technique for the concentration determination of species (e.g., methane and water vapor) in gaseous flows. It belongs to the class of laser absorption spectroscopy-based techniques exploiting the resonance of a coherent laser with the photon energy of a specific molecule in combination with the use of tuneable diode lasers.

In particular, the wavelength of the diode laser is tuned over a particular absorption line of interest, and the intensity of the transmitted radiation is measured. Therefore, the concentration of the species is correlated with the transmitted intensity through the Beer–

Lambert law. Furthermore, it becomes an attractive method for velocity measurement by exploiting the well-known “Doppler shift” effect, which can be seen as a shift in the absorption spectrum. This shift in the frequency spectrum is related to the mean flow velocity.

Due to its non-intrusive nature, high sensitivity, high signal-to-noise ratio (SNR), fast response, and compactness, TDLAS is suitable for the harsh environment of supersonic flows. Hence, it offers a robust diagnostic technique for combustion diagnostics of real engines and propulsions systems. In this regard, TDLAS has been recently applied to measure flow velocity in propulsion engines [49]. For instance, Yao [50] conducted TDLAS experiments to measure the plume velocity of a solid rocket motor (SRM). Similarly, in [51] three solid propellants, i.e., double-base (DB), composite-modified double-base (CMDB), and nitrate ester plasticized polyether (NEPE), were burned in an SRM with an internal diameter of 50 mm. TDLAS measurements of the plume velocity were performed through a scanned wavelength-modulation absorption spectrum with second harmonic detection (SWMS-2f). This last approach was also used to detect the presence of water vapor in a solid rocket motor plume [52], by measuring the vibrational transitions.

9. Experimental Techniques Comparison and Conclusions

The previous sections have provided a comprehensive overview concerning the use of different non-intrusive techniques to characterize SRM’s plume. Their implementation results from a trade-off between multiple variables, which must consider different physical and chemical plume properties as well as the plume characteristics to be measured (e.g., temperature, velocity, density, chemical species). Furthermore, the use and the choice of each experimental method also depend on the geometrical scale, ranges of flow temperature, pressure and velocity, chemical species, and testing environment.

The emissivity-based techniques have been applied to a large range of applications at both the laboratory and real SRM scale. They have been used in both local and global measurements, using proper modifications of the optical system involved in the measurement process (for instance using or not using a cosine corrector at the head of an optical fiber).

Among them, infrared imaging has demonstrated a strong flexibility due to its capability to operate with the large IR emissivity of SRM plumes. The captured radiation signature of the plume allows for the detection of the modification of the plume structures in combination with the presence of condensed phases in the propellant, such as alumina particles.

Spectroscopic methods (UV–VIS and FTIR) are more prone to species identification and alumina temperature quantification, due to its non-intrusive nature, high SNRs, simultaneous monitoring of multiple species, the absence of a sampling system, and compactness and portability of the whole measurement system, allowing for application in real engine test facilities.

Digital inline holography (DIH) has been also applied at the laboratory scale for 3D imaging and quantification of alumina size distribution in solid rocket grains burning at atmospheric pressure. However, it fails when applied to real-scale SRM supersonic plumes due to susceptibility of the laser-derived image degradation via index-of-refraction gradients. Therefore, to date, it is still not suitable for measurements in the harsh environment created by the combustion of an aluminized solid-rocket fuel.

To capture the density variation due to thermal gradients and pressure waves occurring in a supersonically expanding compressible flow, the techniques based on the variation of the refraction index, such as Schlieren and shadowgraphy, have shown the best results, due to the direct relationship between the refractive index and the density. Such density-based methods are imaging techniques, and their sensitivity, accuracy, and precision are affected by the coupling between the technical properties of the camera and optical systems and the thermophysical properties of the investigated plume.

In this regard, the use of a double pass setup has demonstrated an improved capability in amplifying the effect of the density variation on the deflection of the light. Furthermore, in applications to real-scale SRM operating in the ambient light environment, the most recent instruments commercially available can digitally filter the acquired image for environmental noise removal with functionalities such as "dark function", for instance.

The working field of the variation index techniques, and in some optical configurations, as BOS, could be easier applied to full-scale testing systems, as in supersonic jets, by revealing the flow density gradient.

Among the density-based techniques, the background-oriented Schlieren (BOS), also known as digital Schlieren, has a significantly reduced technical complexity providing high-portability and the minimization of the natural background noise due to the use of a retro-reflective target. Furthermore, unlike the traditional Schlieren, the BOS does not use any mirror, which allows for enlarging the field-of-view required to observe full-scale supersonic plume. In comparison with the classical Schlieren, BOS needs more complex post-processing, which includes the application of FFT-based image cross-correlation to compute the optical displacement field induced by the Schlieren effect, followed by the solution of the ray-tracing problem to convert it to the density field. This leads to an increased computational cost (typically more than 30 s to process a megapixel-range image pair). Another disadvantage of the BOS is that its resolution is strictly related to the resolution of the optical displacement field retrieved by cross-correlating the distorted and undistorted images of the target. Therefore, the density gradient resolution is limited not only by the spatial resolution of the image but also by the size of the interrogation windows of the cross-correlation algorithm, and the design of a high-resolution target becomes of primary importance. Any undesired small vibration of the camera or target can introduce errors and uncertainty in the density measurement due to fictitious optical displacements. A novel variant of a mirrorless Schlieren is represented by the focusing Schlieren, which has been used to deal with the limiting characteristics of the conventional Schlieren system and to reduce the influence of non-pertinent flow features and extend larger fields of view, due to the use of a retro-reflective source grid in combination with a specular cut-off grid.

Table 1 summarizes these main findings with particular focus on the measured properties or variables, class of accuracy, working field, and test case scale.

Table 1. Experimental techniques for SRM plume characterization: comparison.

Technique	Revealed Quantity	Accuracy	Working Field	Working Scale
Spectroscopy (UV–VIS)	Chemical composition (mainly $Al_2O_{3)}$	High—Quantitative	High temperature (>1000 K [53])	Laboratory scale/Full-scale real conditions
IR signature	Chemical composition and temperature (mainly CO_2 and H_2O)	High—Quantitative	High temperature (>1000 K [53])	Laboratory scale/Full-scale real conditions
Schlieren Technique	Refraction index gradient	Qualitative Ultra-high precision surface finish and durable optical coatings need to provide accurate Schlieren image. A $3\lambda/2$ mirror surface accuracy ensures a good image.	The density range and the spatial resolution depend on the overall optical setup and the scale of the flow.	Laboratory scale/Full-scale real conditions
Shadowgraph	Refraction index Laplacian	Qualitative	Density variation presence	Laboratory scale/Full-scale real conditions
BOS	Refractive index	Low—Quantitative Increased accuracy by using background patterns with continuously changing random dots (e.g., speckle pattern) and advanced processing algorithms.	The density range and the spatial resolution depend on the overall optical setup and the scale of the flow.	Laboratory scale/Full-scale real conditions
Digital Inline Holography	Particle Dimensions	High—Quantitative	Detectable particles in relation to optics characteristics (the typical pixel pitch currently is about 7 μm)	Laboratory scale
TDLAS	Species concentration and velocity	High—Quantitative Plume velocity measurement with a relative standard deviation below 4% [51].	Gaseous species and tuneable diode laser light source.	Laboratory scale

Author Contributions: Conceptualization, M.G.D.G. and D.F.; methodology, M.G.D.G. and D.F.; formal analysis, A.M.T., M.R.L., D.F. and M.G.D.G.; writing—original draft preparation, A.M.T., M.R.L. and D.F.; writing—review and editing, M.G.D.G.; supervision, M.G.D.G.; project administration, M.G.D.G.; funding acquisition, M.G.D.G. All authors have read and agreed to the published version of the manuscript.

Funding: This project received funding from the PON GENERAZIONE E (Cod. ARS01_011318) PNR 2015-2020.

Institutional Review Board Statement: Not applicable.

Informed Consent Statement: Not applicable.

Acknowledgments: We thank eng. Sabina Spagnolo for assistance during the construction of the experimental set-up and testing activities.

Conflicts of Interest: The authors declare no conflict of interest.

References

1. Ross, M.N.; Danilin, M.Y.; Weisenstein, D.K.; Ko, M.K.W. Ozone depletion caused by NO and H2O emissions from hydrazine-fueled rockets. *J. Geophys. Res. Earth Surf.* **2004**, *109*. [CrossRef]
2. Beier, K.; Lindermeir, E. Comparison of line-by-line and molecular band IR modeling of high altitude missile plume. *J. Quant. Spectrosc. Radiat. Transf.* **2007**, *105*, 111–127. [CrossRef]
3. Aiyan, G.; Tingzhu, B.; Haihe, H.; Yi, T. Analysis of Ultraviolet Radiation Characteristics of Solid Propellant Rocket Motor Exhaust Plume. *Acta Opt. Sin.* **2012**, *32*, 1016002. [CrossRef]
4. Beckstead, M.W.; Puduppakkam, K.; Thakre, P.; Yang, V. Modeling of combustion and ignition of solid-propellant ingredients. *Prog. Energy Combust. Sci.* **2007**, *33*, 497–551. [CrossRef]
5. De Luca, L.T.; Galfetti, L.; Severini, F.; Meda, L.; Marra, G.; Vorozhtsov, A.B.; Sedoi, V.S.; Babuk, V.A. Burning of Nano-Aluminized Composite Rocket Propellants. *Combust. Explos. Shock Waves* **2005**, *41*, 680–692. [CrossRef]
6. Galfetti, L.; De Luca, L.T.; Severini, F.; Meda, L.; Marra, G.; Marchetti, M.; Regi, M.; Bellucci, S. Nanoparticles for solid rocket propulsion. *J. Phys. Condens. Matter* **2006**, *18*, S1991–S2005. [CrossRef]
7. Jayaraman, K.V.A.K.; Anand, K.V.; Chakravarthy, S.R.; Sarathi, R. Effect of nano-aluminium in plat-eau-burning and catalyzed composite solid propellant combustion. *Combust. Flame* **2009**, *156*, 166–1673. [CrossRef]
8. De Luca, L.T.; Shimada, T.; Sinditskii, V.P.; Calabro, M. (Eds.) *Chemical Rocket Propulsion: A Comprehensive Survey of Energetic Materials*; Springer: Berlin/Heidelberg, Germany, 2016; pp. 191–234.
9. Li, Z.; Wang, N.; Shi, B.; Li, S.; Yang, R. Effects of particle size on two-phase flow loss in aluminized solid rocket motors. *Acta Astronaut.* **2019**, *159*, 33–40. [CrossRef]
10. Ko, J.Y.; Lee, E.; Kwon, S. Influence of optical properties of alumina particles on the radiative base heating from solid rocket plume. *Adv. Space Res.* **2019**, *64*, 514–526. [CrossRef]
11. Kuzmin, V.A.; Maratkanova, E.I.; Zagray, I.A.; Rukavishnikova, R.V. Thermal radiation of heterogeneous combustion products in the model rocket engine plume Thermophys. *Aeromech* **2015**, *22*, 371–386. [CrossRef]
12. Parry, D.L.; Brewster, Q.M. Optical constants of Al_2O_3 smoke in propellant flames. *J. Thermophys Heat Transfer.* **1991**, *5*, 142–149. [CrossRef]
13. Sarou-Kanian, V.; Rifflet, J.C.; Millot, F. IR radiative properties of solid and liquid alumina: Effects of temperature and gaseous environment. *Int. J. Thermophys.* **2005**, *26*, 1263–1275. [CrossRef]
14. Plastinin, Y.; Sipatchev, H.; Karabadzhak, G.; Khmelinin, B.; Khlebnikov, A.; Shishkin, Y. Influence of alumina particles' phase transition on its radiation in the middle infrared and ultraviolet regions of spectrum. In Proceedings of the 38th Aerospace Sciences Meeting and Exhibit, Reno, NV, USA, 10–13 January 2000. [CrossRef]
15. Bakhir, L.P.; Levashenko, G.I.; Tamanovich, V.V. Refinement of the imaginary part of the complex refractive index of liquid aluminum oxide. *J. Appl. Spectrosc.* **1997**, *26*, 378–383. [CrossRef]
16. Van der Hulst, H.C. *Light Scattering by Small Particles*; John Wiley & Sons Inc.: New York, NY, USA, 1957.
17. Bityukov, V.K.; Petrov, A.V. Absorption coefficient of molten aluminum oxide in semitransparent spectral range. *Appl. Phys. Res.* **2013**, *5*, 51. [CrossRef]
18. Jackson, T.L.; Najjar, F.; Buckmaster, J. New aluminum agglomeration models and their use in solidpropellant-rocket sim-ulations. *J. Propuls. Power* **2005**, *21*, 925–936. [CrossRef]
19. Lengell'e, G.; Duterque, J.; Trubert, J.F. Combustion of solid propellants. In Proceedings of the RTO/VKI Special Course on Internal Aerodynamics in Solid Rocket Propulsion, Rhode-Saint-Genèse, Belgium, 27–31 May 2002; pp. 1–62, published in RTO-EN-023-4.
20. Karasev, V.; Onischuk, A.; Glotov, O.; Baklanov, A.; Maryasov, A.; Zarko, V.; Panfilov, V.; Levykin, A.; Sabelfeld, K. Formation of charged aggregates of Al2O3 nanoparticles by combustion of aluminum droplets in air. *Combust. Flame* **2004**, *138*, 40–54. [CrossRef]

21. Reed, R.; Calia, V. Review of aluminum oxide rocket exhaust particles. In Proceedings of the 28th Thermophysics Conference, Orlando, FL, USA, 6–9 July 1993; p. 2819. [CrossRef]
22. Rattenni, L. Solid motor plume analyses for the STAR-1 spacecraft. In Proceedings of the 36th AIAA/ASME/SAE/ASEE Joint Propulsion Conference and Exhibit, Las Vegas, NV, USA, 24–28 July 2000; p. 3190.
23. Sambamurthi, J. Plume particle collection and sizing from static firing of solid rocket motors. In Proceedings of the 31st Joint Propulsion Conference and Exhibit, San Diego, CA, USA, 10–12 July 1995. [CrossRef]
24. Dombrovsky, L.A. *Radiation Heat Transfer in Disperse Systems*; Begell House: New York, NY, USA, 1996.
25. Giechaskiel, B.; Clairotte, M. Fourier Transform Infrared (FTIR) Spectroscopy for Measurements of Vehicle Exhaust Emissions: A Review. *Appl. Sci.* **2021**, *11*, 7416. [CrossRef]
26. Gill, W.; Cruz-Cabrera, A.A.; Donaldson, A.B.; Lim, J.; Sivathanu, Y.; Bystrom, E.; Haug, A.; Sharp, L.; Surmick, D. Combustion diagnosis for analysis of solid propellant rocket abort hazards: Role of spectroscopy. *J. Phys. Conf. Ser.* **2014**, *548*, 012055. [CrossRef]
27. Jörg, H.; Schäfer, K. Analysis of aircraft exhausts with Fourier-transform infrared emission spectroscopy. *Appl. Opt.* **1997**, *36*, 4922–4931.
28. Saile, D.; Allofs, D.; Kühl, V.; Stefens, L.; Gülhan, A.; Beversdorf, M.; Förster, W.; Willert, C.; Carlotti, S.; Maggi, F.; et al. Characterization of SRM plumes with alumina particulate in subscale testing. *CEAS Space J.* **2021**, *13*, 247–268. [CrossRef]
29. Sangmin, K.; Sanghoon, K.; Mintaek, K.; Soonho, S.; Joon, S.L. Infrared signature of NEPE, HTPB rocket plume under varying flight conditions and motor size. *Infrared Phys. Technol.* **2021**, *112*, 103590.
30. Qinglin, N.I.U.; Zhihong, H.E.; Shikui, D.O.N.G. IR radiation characteristics of rocket exhaust plumes under varying motor operating conditions. *Chin. J. Aeronaut.* **2017**, *30*, 1101–1114.
31. Wang, W.; Li, S.; Zhang, Q.; Wang, N. Infrared radiation signature of exhaust plume from solid propellants with different energy characteristics. *Chin. J. Aeronaut.* **2013**, *26*, 594–600. [CrossRef]
32. Hudson, M.K.; Shanks, R.B.; Snider, D.H.; Lindquist, D.M.; Luchini, C.; Rooke, S. UV, Visible, and Infrared Spectral Emissions in Hybrid Rocket Plumes. *Int. J. Turbo Jet-Engines* **1998**, *15*, 71–87. [CrossRef]
33. Avital, G.; Cohen, Y.; Gamss, L.; Kanelbaum, Y.; Macales, J.; Trieman, B.; Yaniv, S.; Lev, M.; Stricker, J.; Sternlieb, A. Experimental and Computational Study of Infrared Emission from Underexpanded Rocket Exhaust Plumes. *J. Thermophys. Heat Transf.* **2001**, *15*, 377–383. [CrossRef]
34. Devir, A.; Lessin, A.; Cohen, Y.; Yaniv, S.; Kanelbaum, Y.; Avital, G.; Gamss, L.; Macales, J.; Trieman, B.; Lev, M.; et al. Comparison of calculated and measured radiation from a rocket motor plume. In Proceedings of the 39th Aerospace Sciences Meeting and Exhibit, Reno, NV, USA, 8–11 January 2001. [CrossRef]
35. Moran, R.P.; Houston, J.D. Infrared Imagery of Solid Rocket Exhaust Plumes. In Proceedings of the JANNAF 8th Modeling and Simulation Subcommittee Meeting, Huntsville, AL, USA, 5–9 December 2011.
36. Settles, G.S. *Schlieren and Shadowgraph Techniques: Visualizing Phenomena in Transparent Media*; Springer: Berlin, Germany, 2001.
37. Merzkirch, W. Techniques of Flow Visualization. In *NORTH ATLANTIC TREATY ORGANIZATION—Advisory Group for Aerospace Research and Development*; Institut für Thermo und Fluiddynamik Ruhr-Universität Bochum: Bochum, Germany, 1987; AGARDograph No. 302.
38. Hargather, M.J.; Settles, G.S. Recent Developments in Schlieren and Shadowgraphy. In Proceedings of the 27th AIAA Aerodynamic Measure-ment Technology and Ground Testing, Chicago, IL, USA, 28 June–1 July 2010.
39. Zhou, Z.; Bao, Y.; Sun, P.; Li, Y. Cooling of rocket plume using aqueous jets during launching. *Eng. Appl. Comput. Fluid Mech.* **2021**, *16*, 20–35. [CrossRef]
40. Hooke, R. *Micrographia: Or, Some Physiological Descriptions of Minute Bodies Made by Magnifying Glasses. With Observations and Inquiries Thereupon*; Martyn and Allestry: London, UK, 1665.
41. Krehl, P.; Engemann, S. August Toepler—The First Who Visualized Shock Waves. *Shock Waves* **1995**, *5*, 1–18. [CrossRef]
42. Cauty, F.; Eradès, C.; Desse, J.-M. Light deviation based optical techniques applied to solid propellant combustion. *Prog. Propuls. Phys.* **2011**, *2*, 121–134. [CrossRef]
43. Frey, M.; Makowka, K.; Aichner, T.; Stark, R.; Génin, C. The TICTOP nozzle—First experimental results. In Proceedings of the 7th European Conference for Aeronautics and Space Sciences (EUCASS), Milan, Italy, 3–6 July 2017.
44. Kolář, J. Error analysis of supersonic air-to-air ejector schlieren pictures. *EPJ Web Conf.* **2013**, *45*, 1004. [CrossRef]
45. Maeda, H.; Fukuda, H.; Nakao, S.; Miyazato, Y.; Ishino, Y. Rainbow schlieren measurements in underexpanded jets from square supersonic micro nozzles. *EPJ Web Conf.* **2018**, *180*, 02058. [CrossRef]
46. Wernet, M.P.; Stiegemeier, B.R. Application of background oriented schlieren for altitude testing of rocket engines. In *National Aeronautics and Space Administration*; Glenn Research Center: Cleveland, OH, USA, 2017.
47. Hargather, M.J.; Lawson, M.; Settles, G.S.; Weinstein, L.M. Seedless Velocimetry Measurements by Schlieren Image Velocimetry. *AIAA J.* **2011**, *49*, 611–620. [CrossRef]
48. Chen, Y.; Guildenbecher, D.R.; Hoffmeister, K.N.G.; Cooper, M.A.; Stauffacher, H.L.; Oliver, M.S.; Washburn, E.B. Study of aluminum particle combustion in solid propellant plumes using digital in-line holography and imaging pyrometry. *Combust. Flame* **2017**, *182*, 225–237. [CrossRef]
49. Chang, L.S.; Strand, C.L.; Jeffries, J.B.; Hanson, R.K.; Diskin, G.S.; Gaffney, R.L.; Capriotti, D.P. Supersonic Mass-Flux Measurements via Tunable Diode Laser Absorption and Nonuniform Flow Modeling. *AIAA J.* **2011**, *49*, 2783–2791. [CrossRef]

50. Yao, L.; Yao, D.; Yi, J.; Kan, R.; Yang, Y.; Xu, Z.; Ruan, J.; Liu, J. Measurement Method of Plume for Solid Propellant Charge Based on TDLAS. *Chin. J. Explos. Propellants* **2016**, *39*, 35–39. [CrossRef]
51. Song, A.; Qin, Z.; Li, J.; Li, M.; Huang, K.; Yang, Y.; Wang, N. Real-Time Plume Velocity Measurement of Solid Propellant Rocket Motors Using TDLAS Technique. *Propellants Explos. Pyrotech.* **2021**, *46*, 636–653. [CrossRef]
52. Almodovar, C.A.; Salazar, D.; Strand, C.L.; Hanson, R.K.; Wright, R.G.; Brophy, C.M. TDLAS Measurements of the Underexpanded Exhaust Plume from a Solid Propellant Gas Generator. In Proceedings of the AIAA Scitech 2019 Forum, San Diego, CA, USA, 7–11 January 2019; p. 0028. [CrossRef]
53. Lynch, P.; Krier, H.; Glumac, N. Emissivity of Aluminum-Oxide Particle Clouds: Application to Pyrometry of Explosive Fireballs. *J. Thermophys. Heat Transf.* **2010**, *24*, 301–308. [CrossRef]